Supporting Information

for *Small*, DOI: 10.1002/smll.201101596

Green Nanochemistry: Metal Oxide Nanoparticles and Porous Thin Films from Bare Metal Powders

*Engelbert Redel, Srebri Petrov , Ömer Dag , Jonathon Moir , Chen Huai , Peter Mirtchev , and Geoffrey A. Ozin **

Submitted to small NANO MICRO

Supporting Information

Green Nanochemistry - Metal Oxide Nanoparticles and Porous Thin Films from bare Metal Powders

*E. Redel[a], S. Petrov[a], Ö. Dag[b], J. Moir[a], C. Huai[a], P. Mirtchev[a], G. A. Ozin[a]**

[a] *Materials Chemistry and Nanochemistry Research Group, Center for Inorganic and Polymeric Nanomaterials, Chemistry Department, 80 St.George Street, University of Toronto, Toronto, M5S 3H6, Ontario, Canada*
[b] *Department of Chemistry, Bilkent University, 06800, Ankara, Turkey*

E-mail: gozin@chem.utoronto.ca

Powder X-Ray Diffraction & Rietfeld refinement

The crystal phase and particle size of the films were analyzed by X-ray diffraction (XRD) using a Siemens D5000 diffractometer and Cu-K□ line as the X-ray source with step scan mode (ss 0.02°, t 2.0 s) in the range of 20–65° 2□. Phase identification was done using Eva™/Search-Match™ routine with PDF-2/2001. The Rietveld refinement was carried out with Bruker AXS general profile fitting software Topas™.

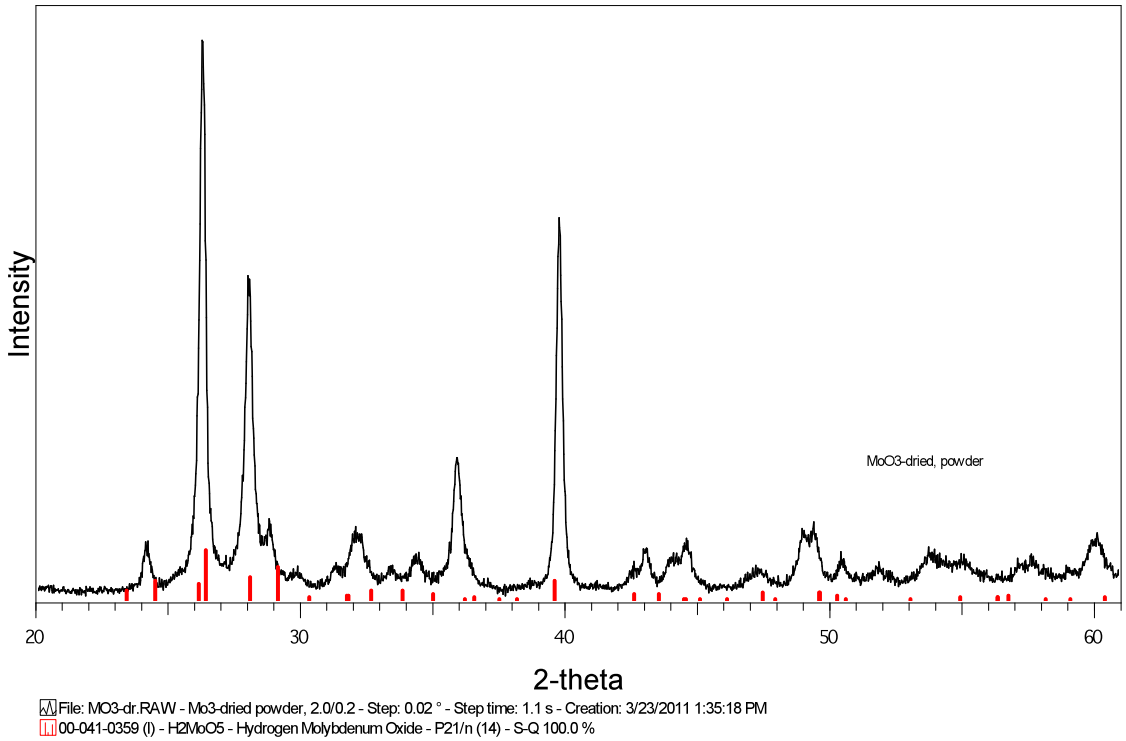

Figure S1: PXRD and Phase analysis of dried MoO_3 dispersion.

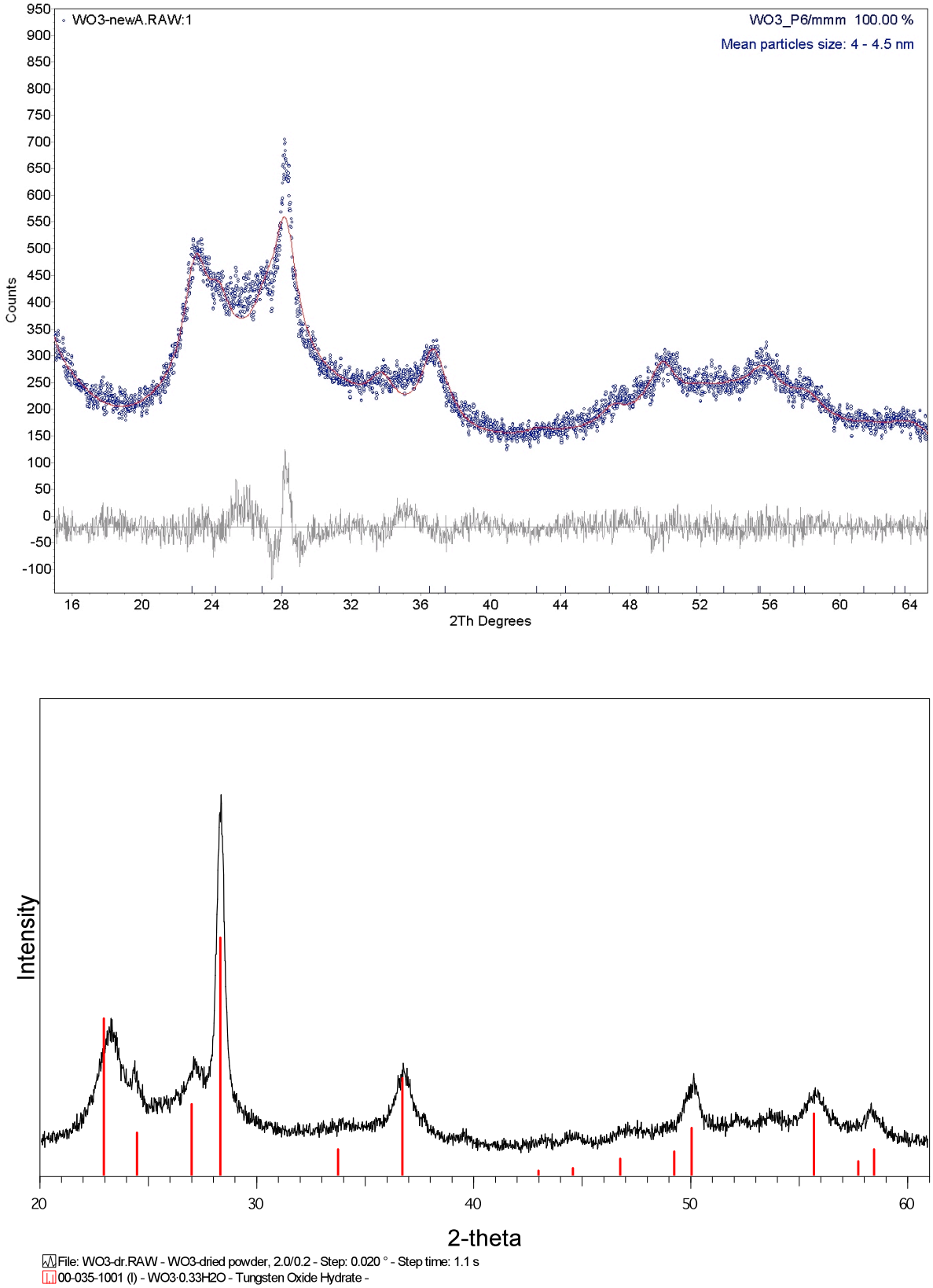

Figure S2: PXRD and Phase analysis of dried WO_3 dispersion.

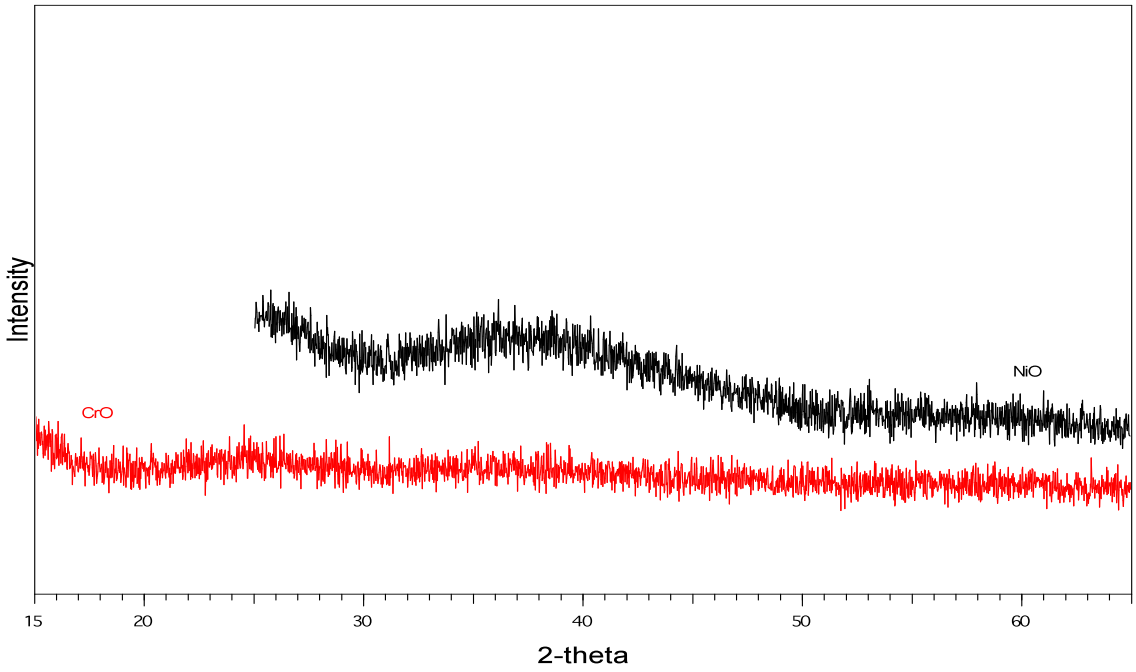

Figure S3: PXRD and Phase analysis of dried Ni- and Co-Oxide dispersions.

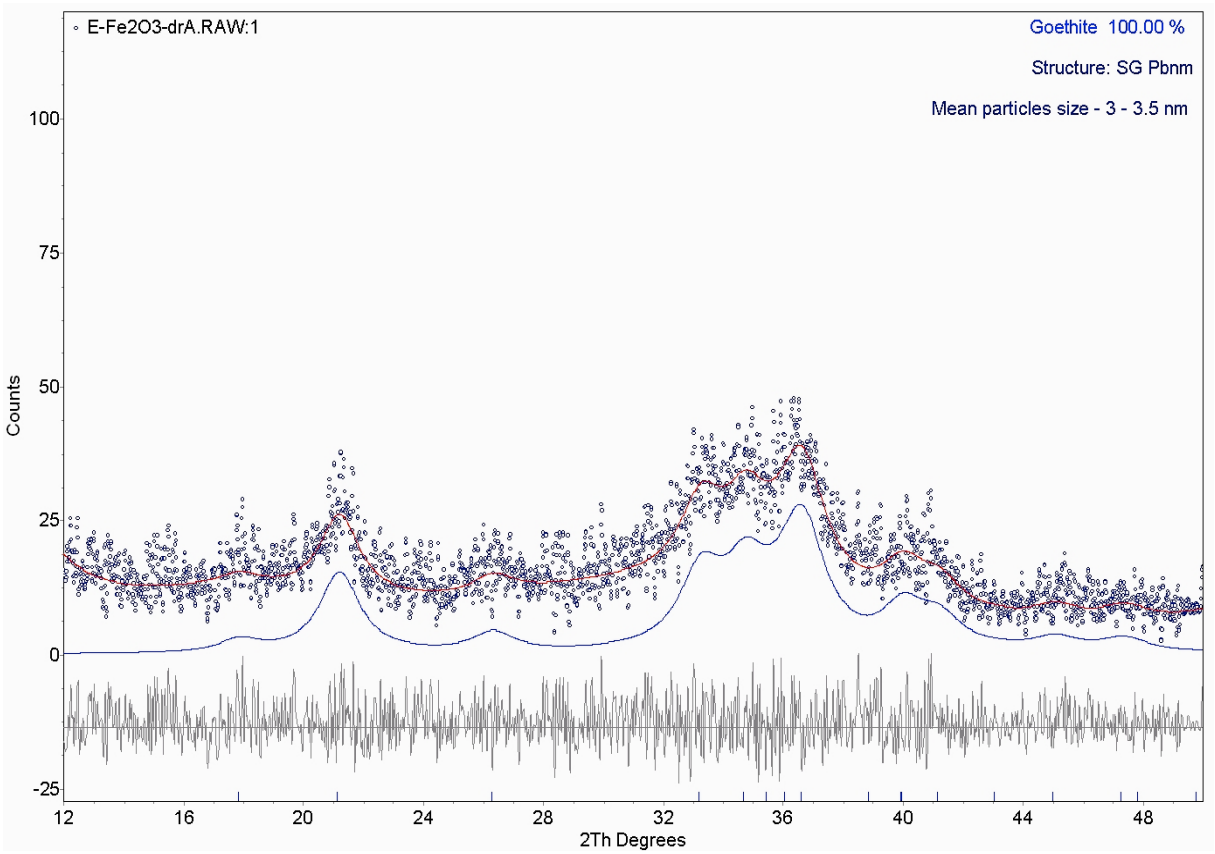

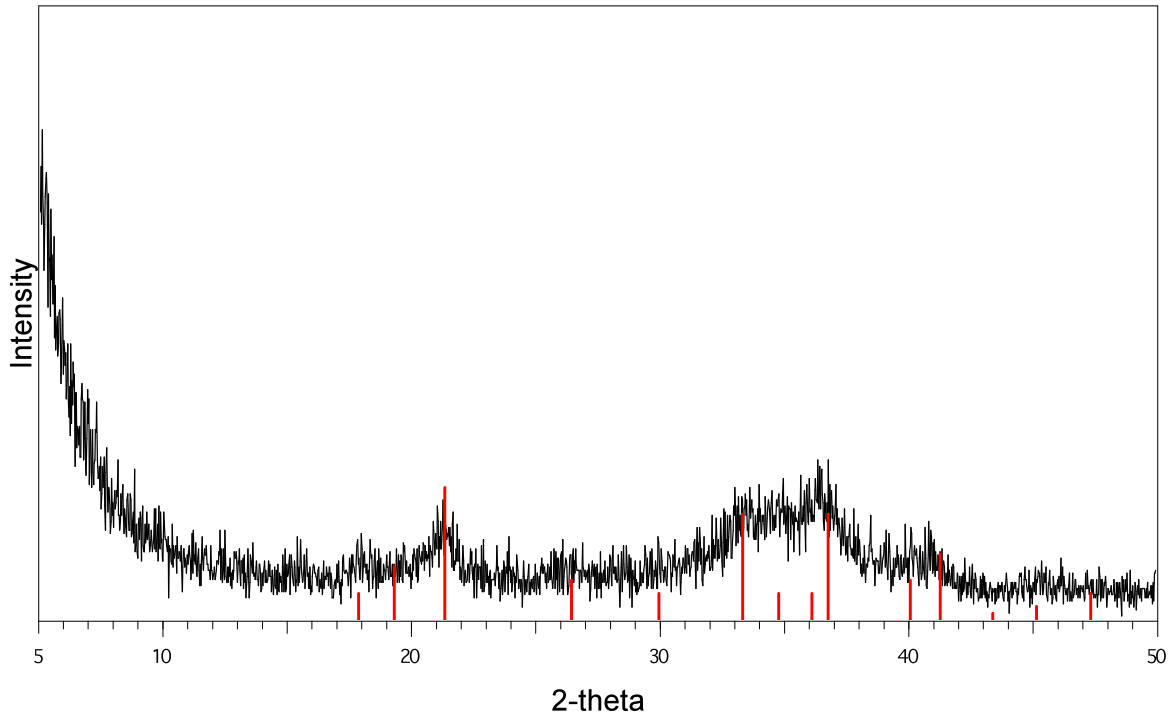

Figure S4: PXRD and Phase analysis of dried Fe_2O_3 dispersion.

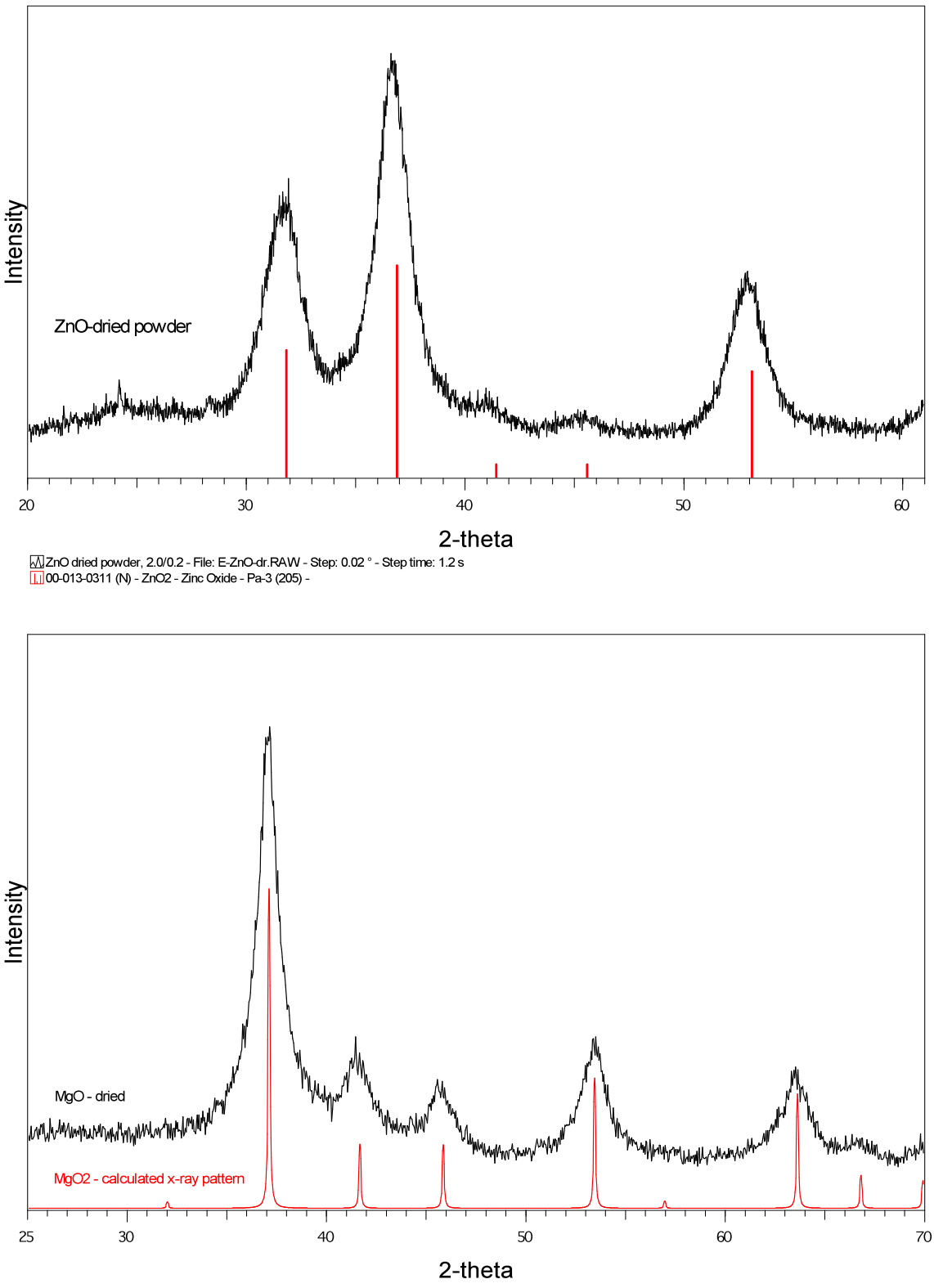

Figure S5: PXRD and Phase analysis of dried ZnO_2 dispersion.

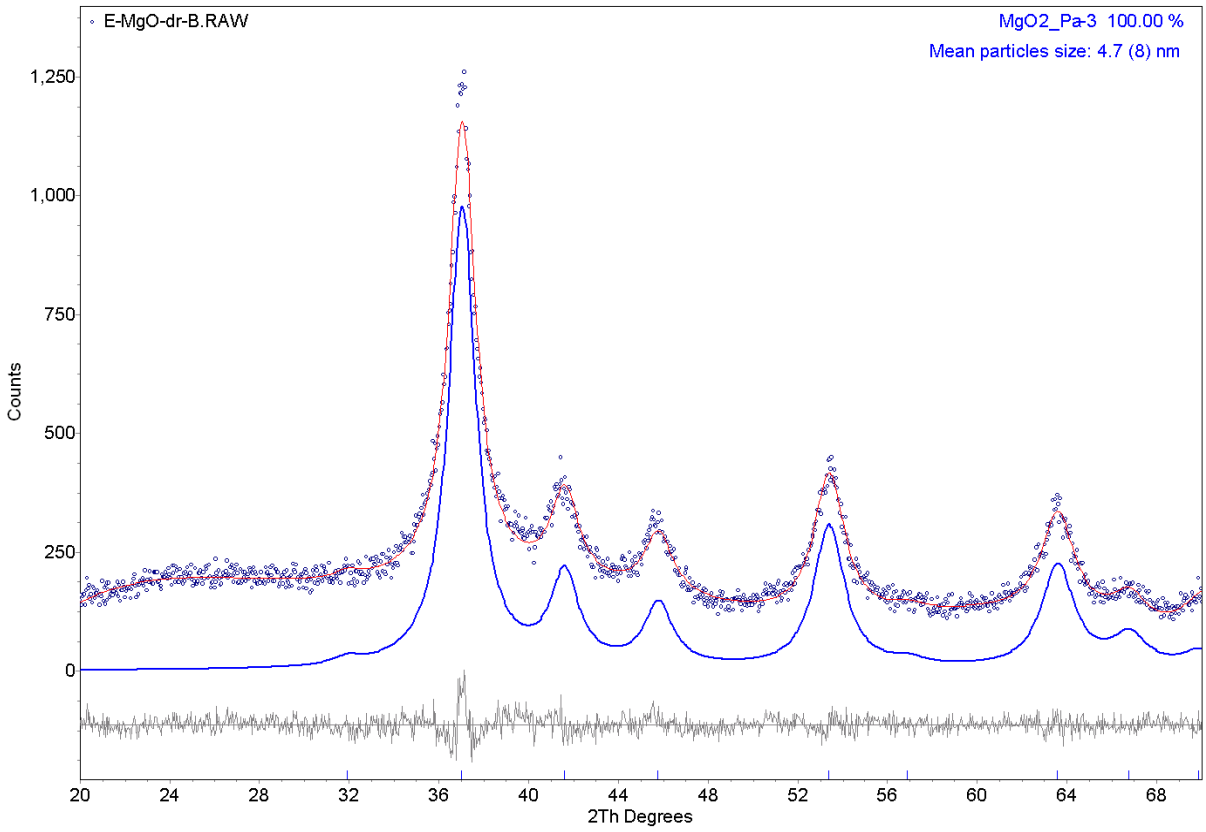

Figure S6: PXRD and Phase analysis of dried MgO_2 dispersion.

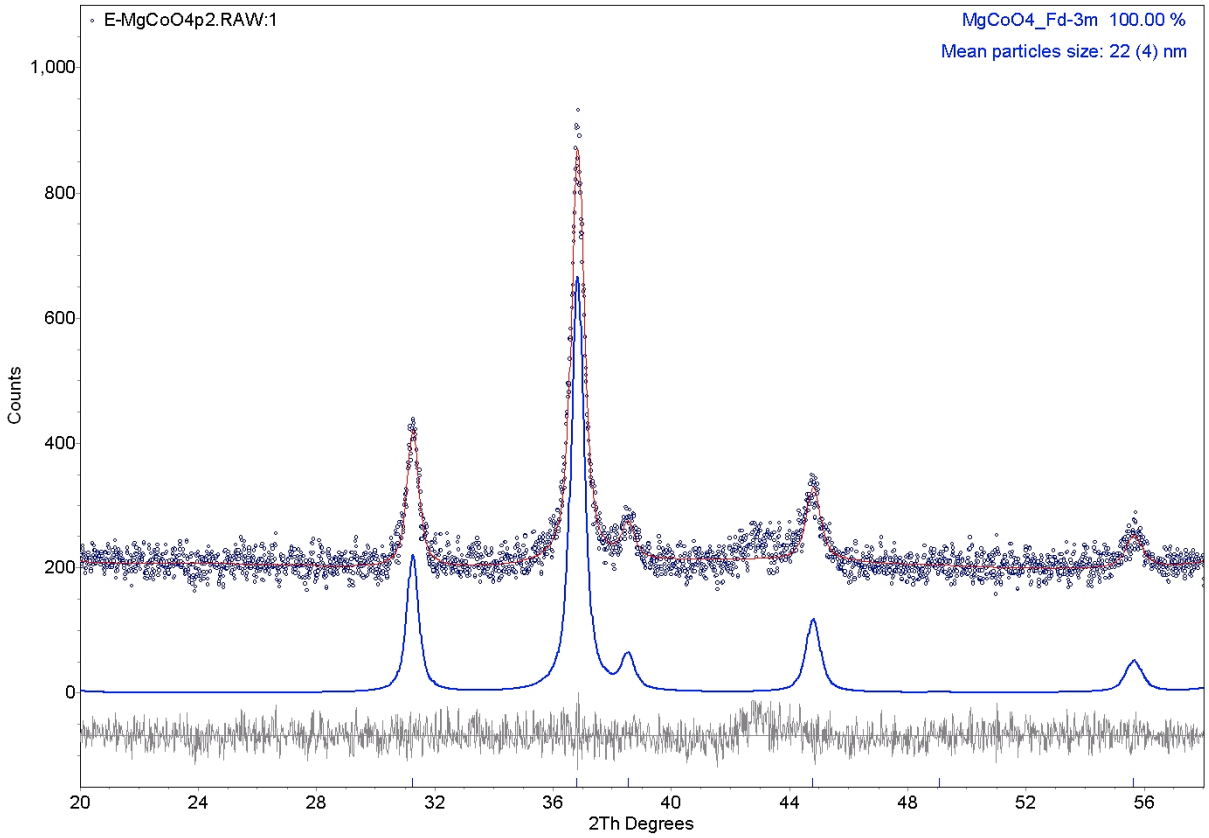

Figure S7: PXRD and Phase analysis of dried $MgCo_2O_4$ dispersion.

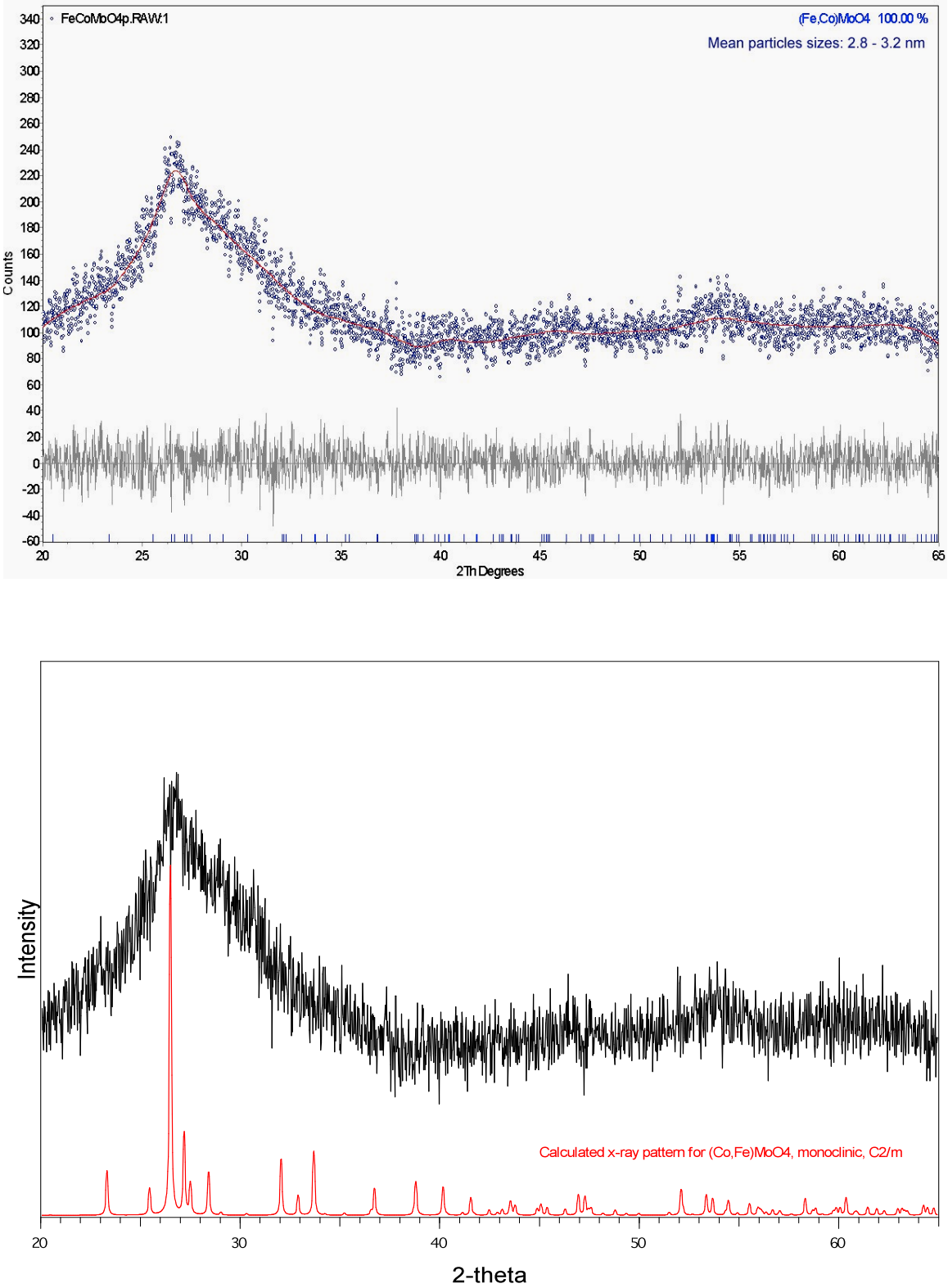

Figure S8: PXRD and Phase analysis of $Fe_{0.3}Co_{0.7}MoO_4$.

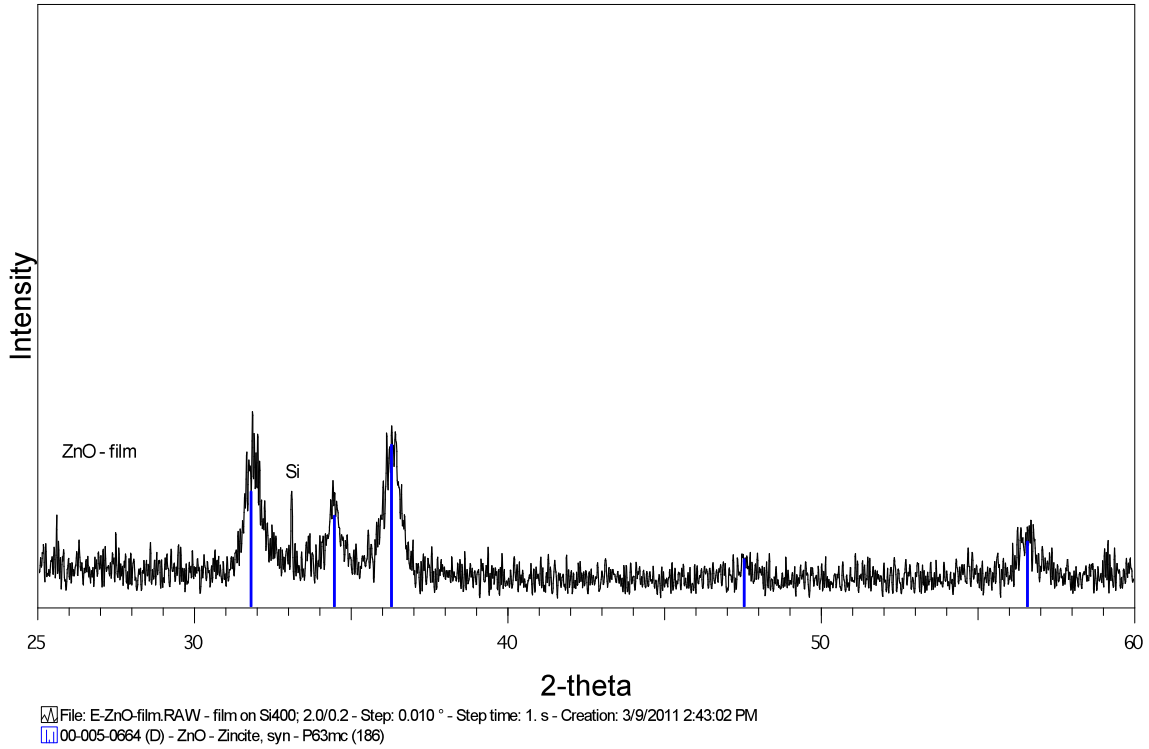

Figure S9: Film-PXRD and Phase analysis of ZnO thin films.

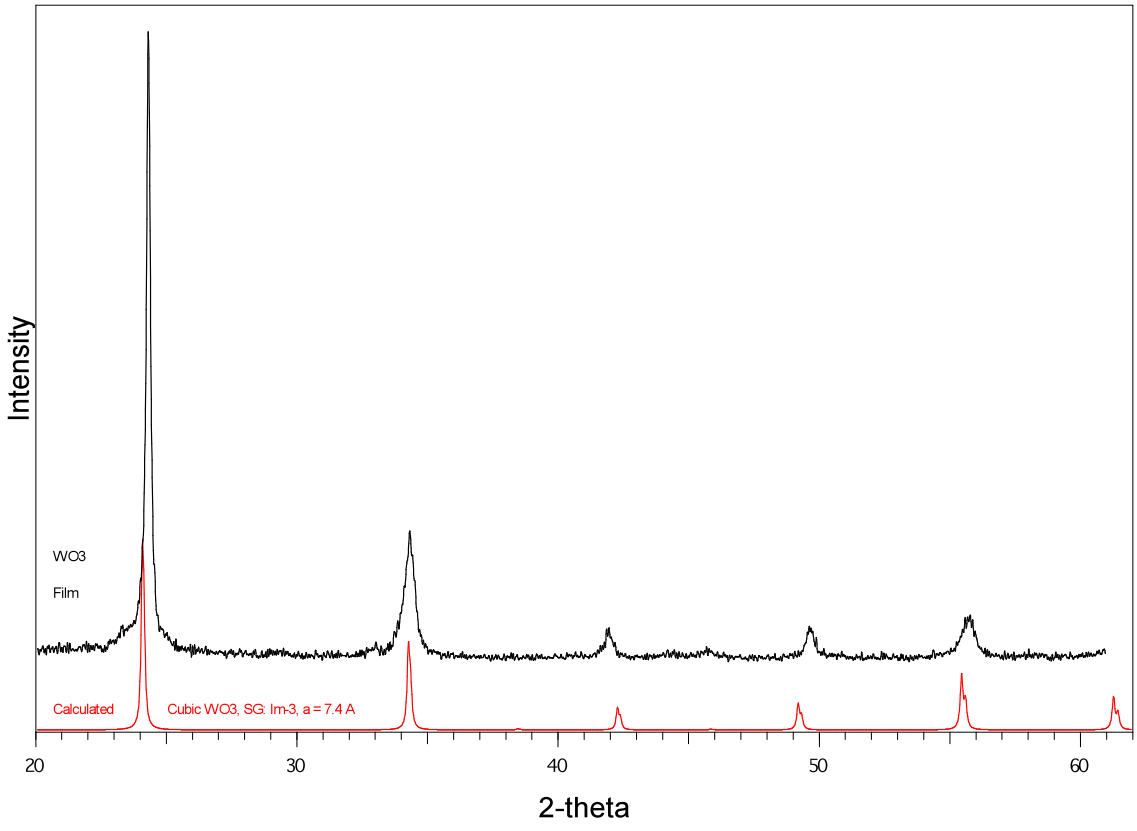

Figure S10: Film-PXRD and Phase analysis of cubic WO_3 thin films.

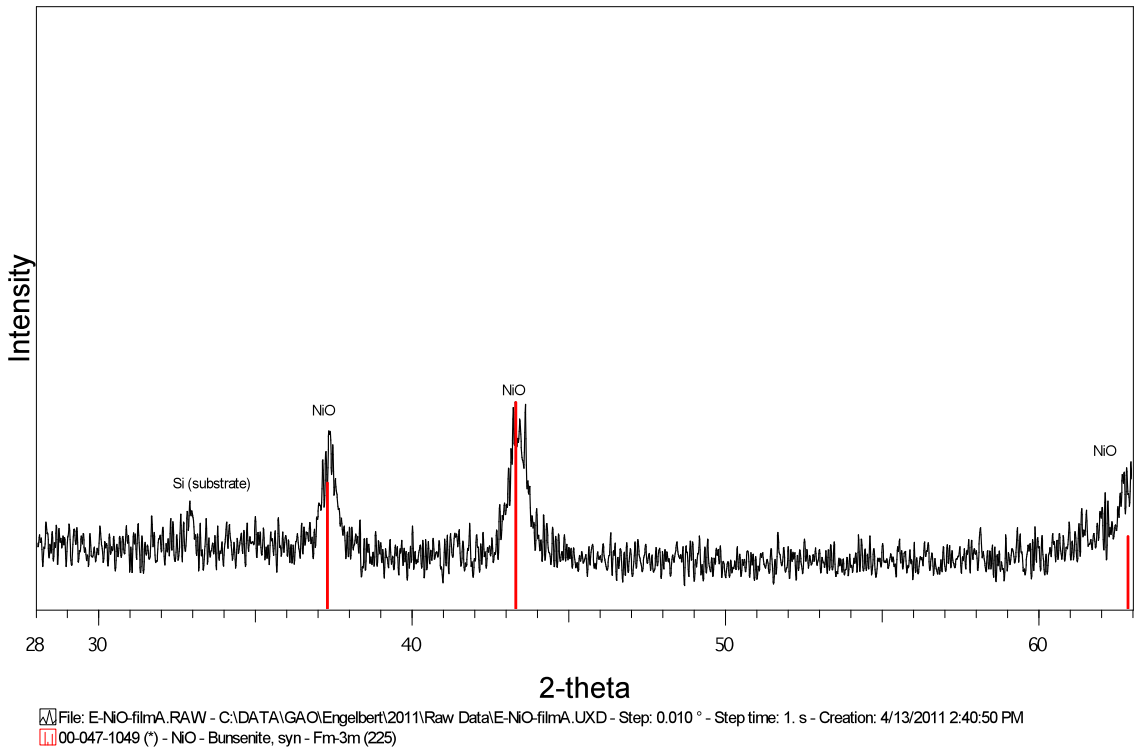

Figure S11: Film-PXRD and Phase analysis of NiO thin films.

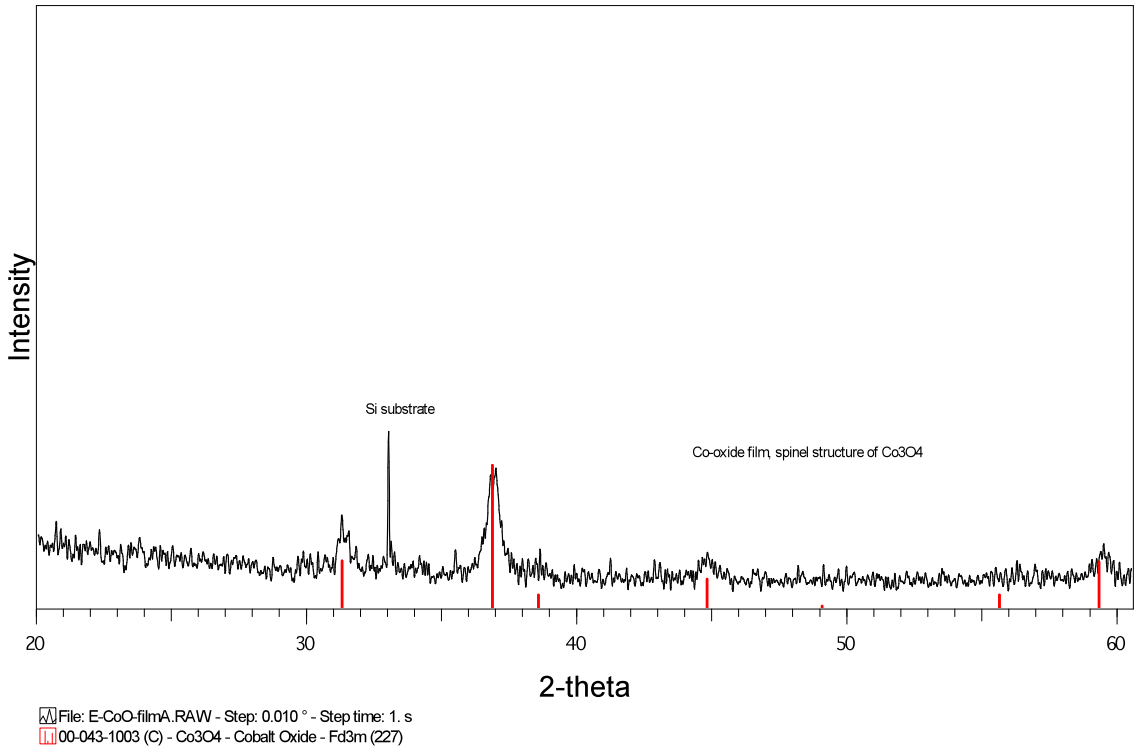

Figure S12: Film-PXRD and Phase analysis of Co_3O_4 thin films.

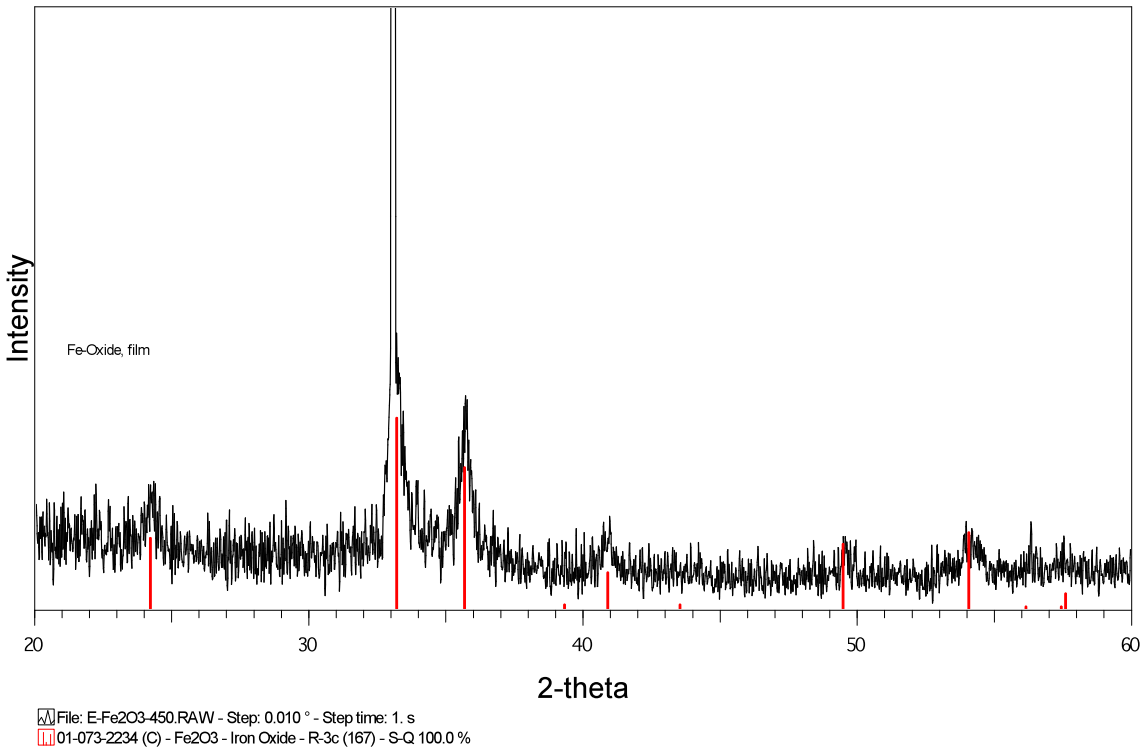

Figure S13: Film-PXRD and Phase analysis of Hematite Fe_2O_3 thin films.

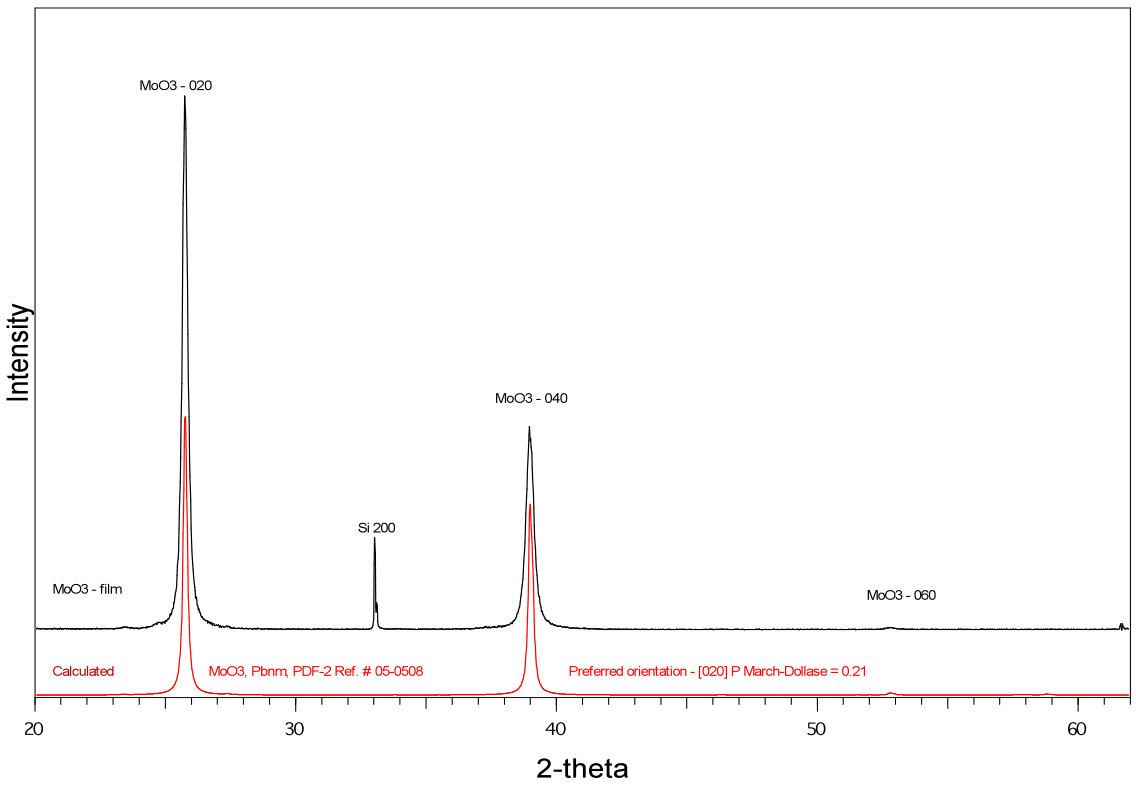

Figure S14: Film-PXRD and Phase analysis of porous MoO_3 thin films.

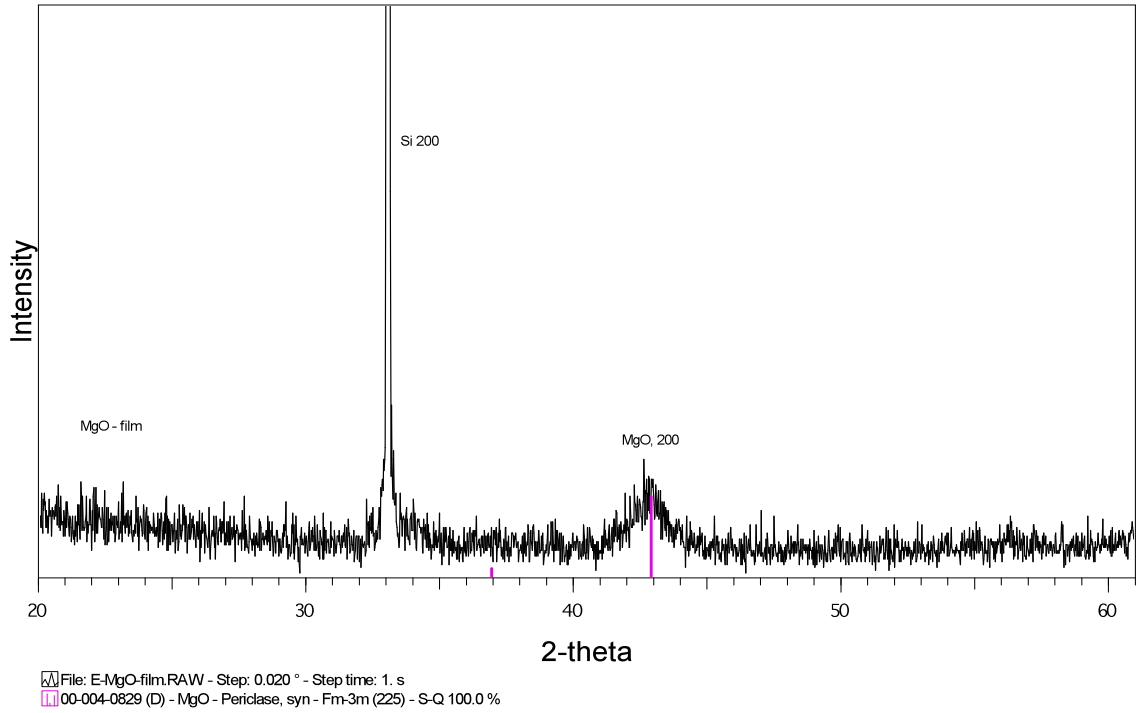

Figure S15: Film-PXRD and Phase analysis of MgO thin films.

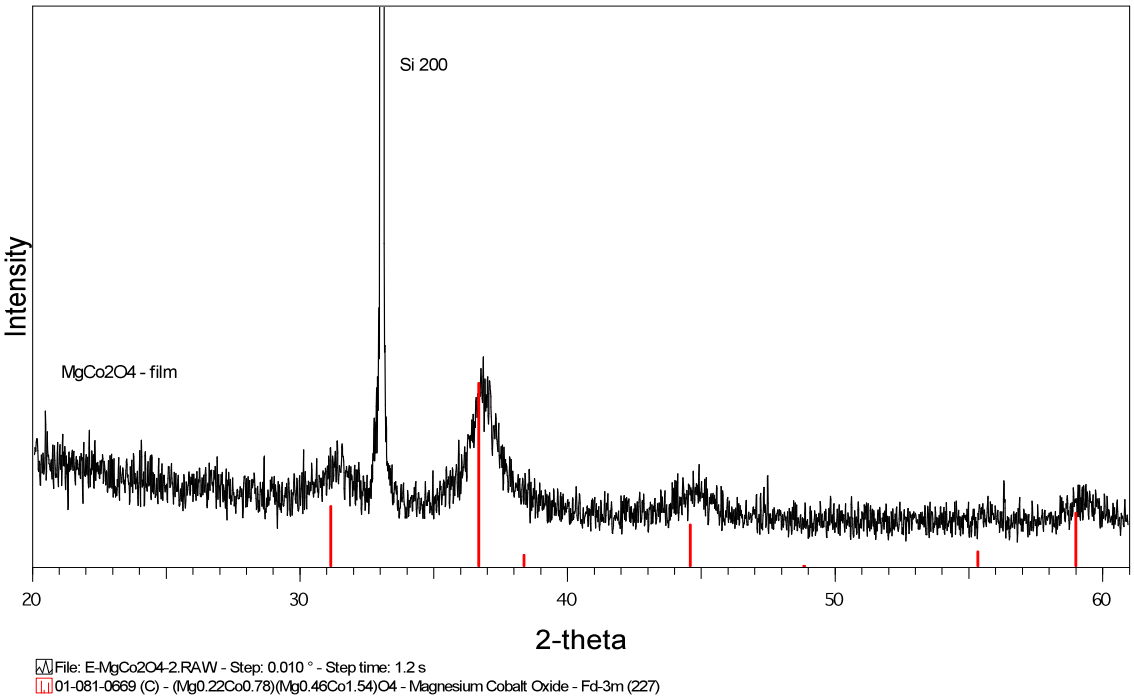

Figure S16: Film-PXRD and Phase analysis of $MgCo_2O_4$ thin films.

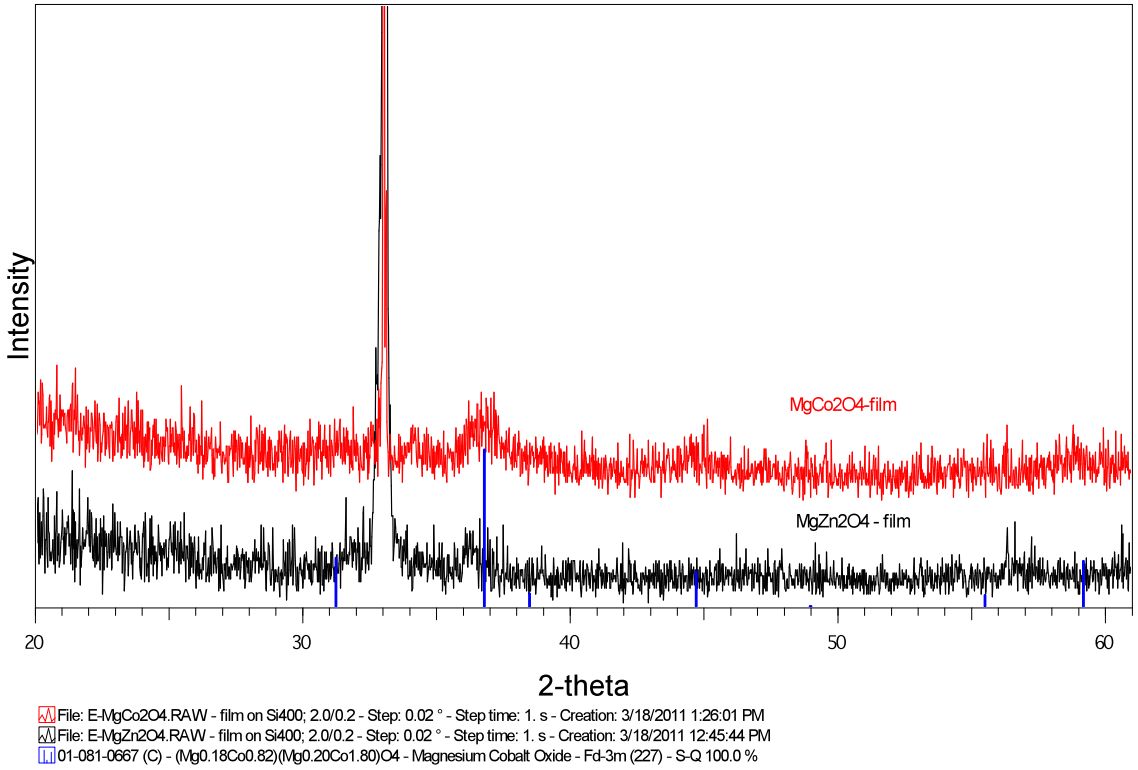

Figure S17: Film-PXRD and Phase analysis of both spinel $MgCo_2O_4$ and $MgZn_2O_4$ thin films.

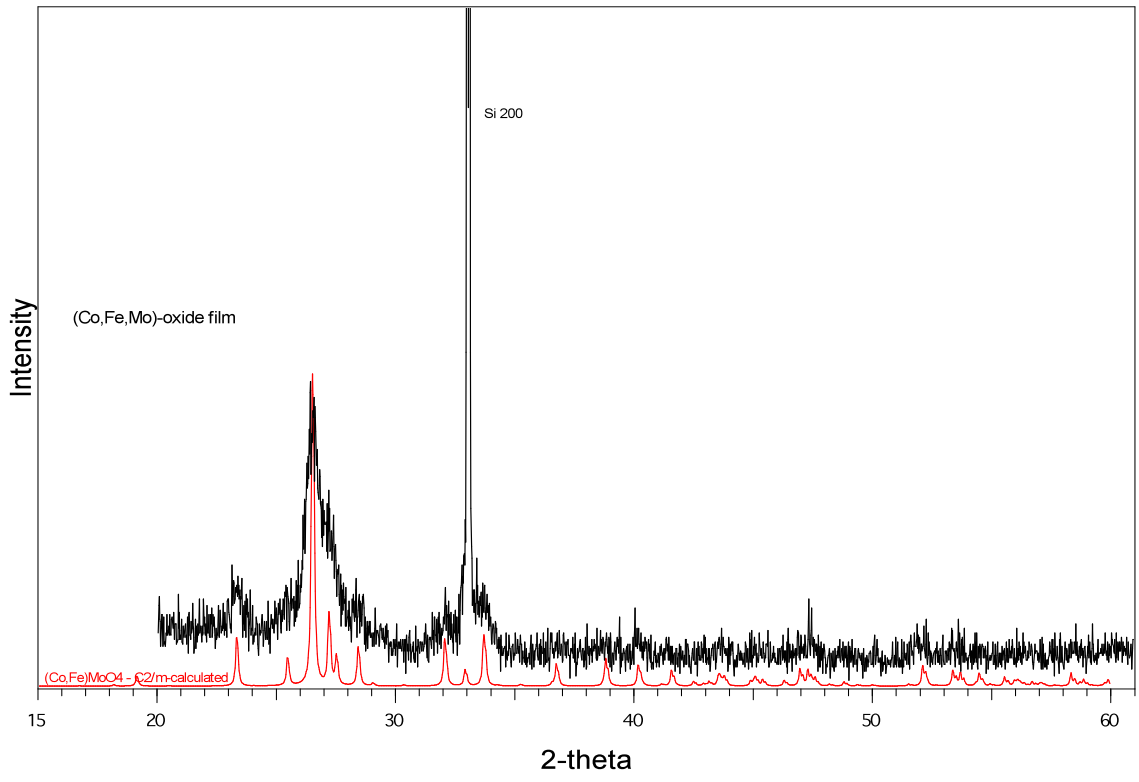

Figure S18: Film-PXRD and Phase analysis of $Fe_{0.3}Co_{0.7}MoO_4$.

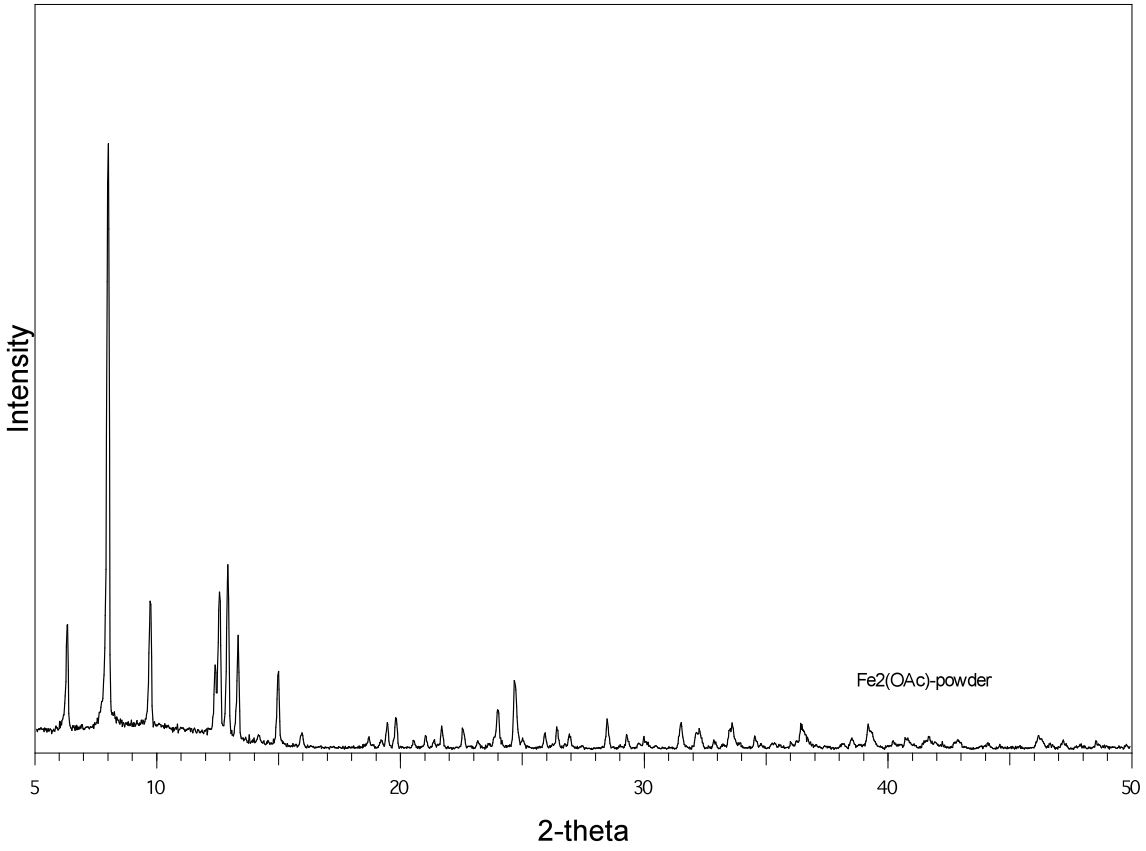

Figure S19: Reference PXRD of powder Fe(II)$(Ac)_2$ salt.

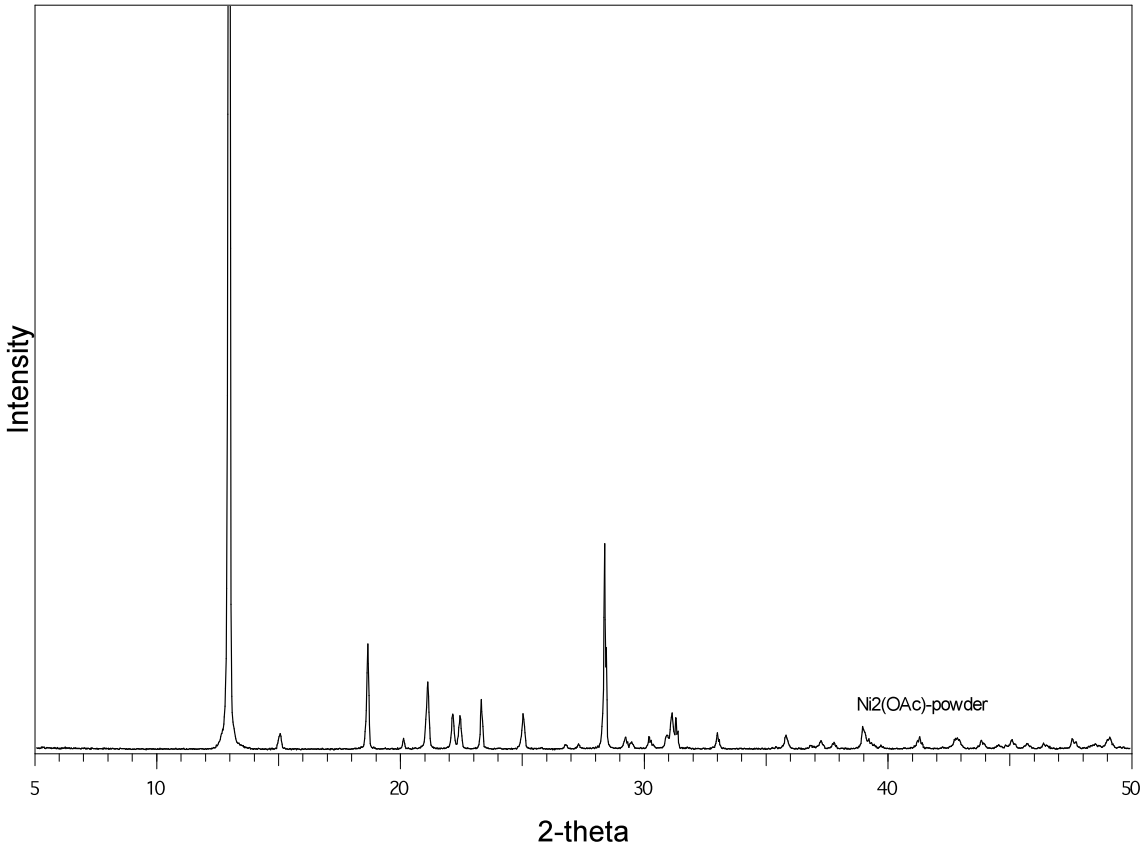

Figure S20: Reference PXRD of powder Ni(II)$(Ac)_2$ salt.

Examples of High-resolution scanning transmission electron microscopy (HR-STEM) were performed on a Hitachi HD-2000 in the Z-contrast mode at an accelerating voltage of 200 kV emission current of 30-50□A. HR-TEM (high-resolution transmission electron microscopy) measurements were performed on a TITAN (FEI) at an accelerating voltage of 300 kV.

The FFT and inverse FFT analysis of a selected area was performed using DigitalMicrograph(TM) Demo 3.6.5. for GMS1 software. The lattice fringes in the images and diffraction spots from the FFT of selected area gave the lattice parameters of the corresponding metal oxides. Those values and the lattice parameters obtained from the Rietveld refinement of the PXRD patterns are consistent with each other.

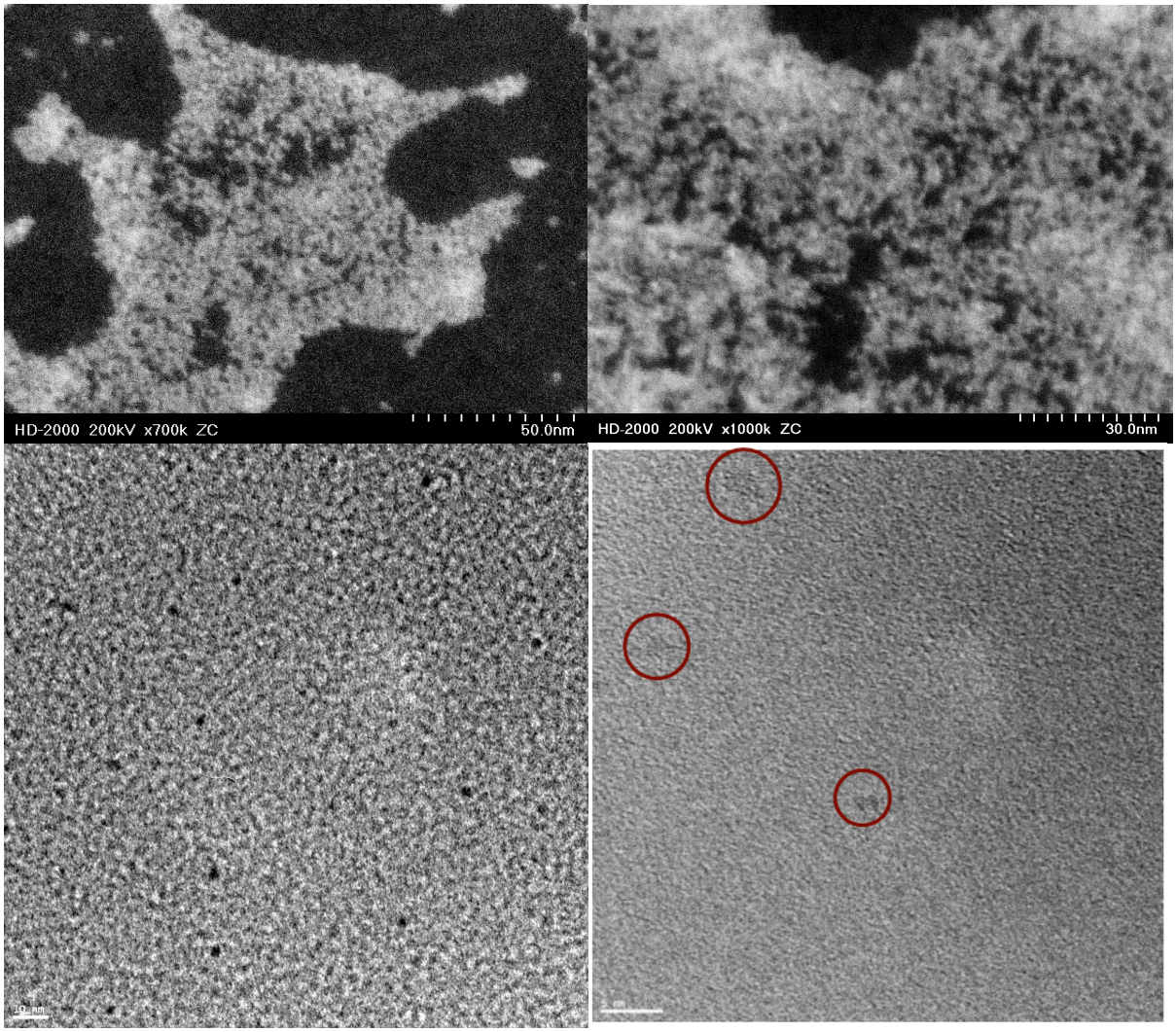

Figure S21: Cryo-STEM and HR-TEM images WO_3 Clusters/NPs from H_2O/H_2O_2 dispersion.

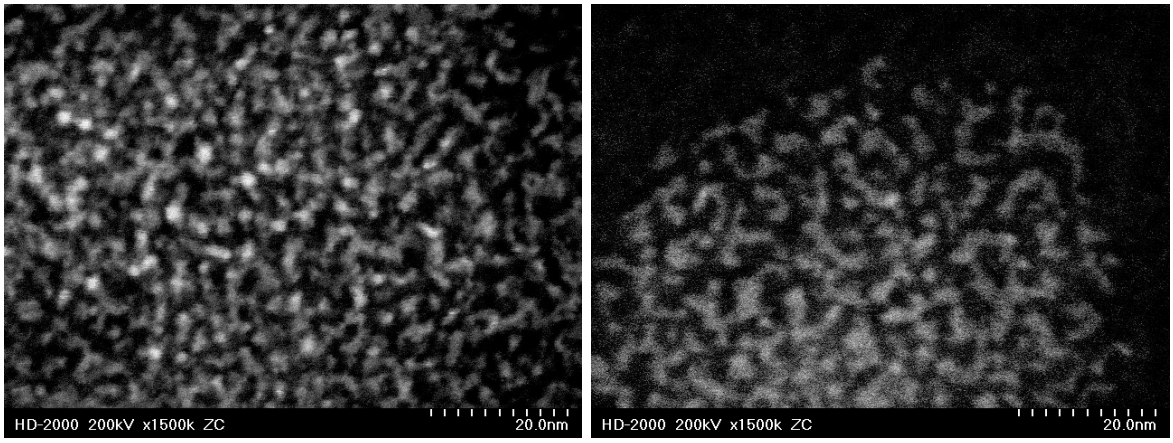

Figure S22: Cryo-STEM images of NiO Cluster/NPs from H_2O/H_2O_2 dispersion.

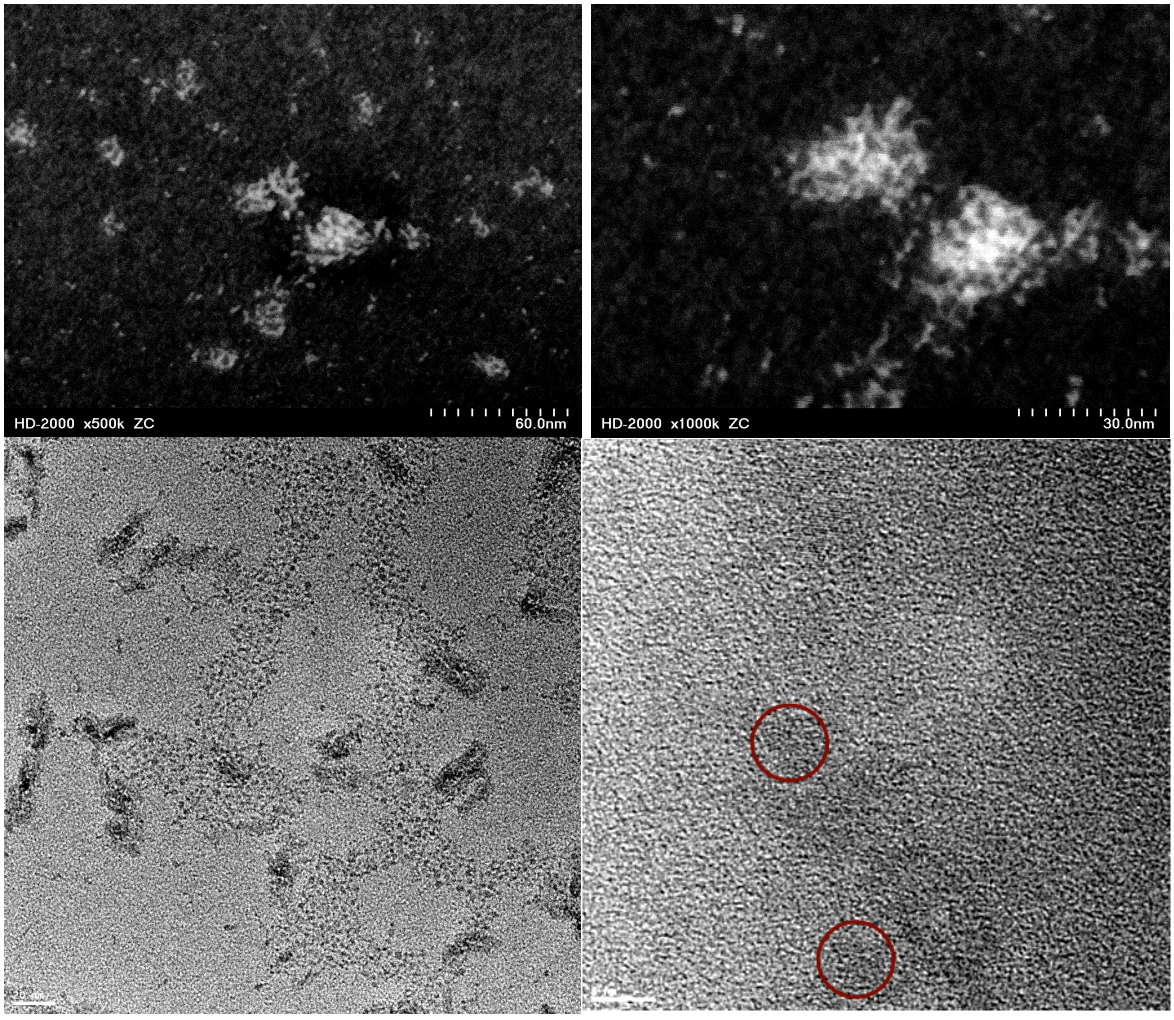

Figure S23: Cryo-STEM and HR-TEM images of Fe_2O_3 of Cluster/NPs from H_2O/H_2O_2 dispersion.

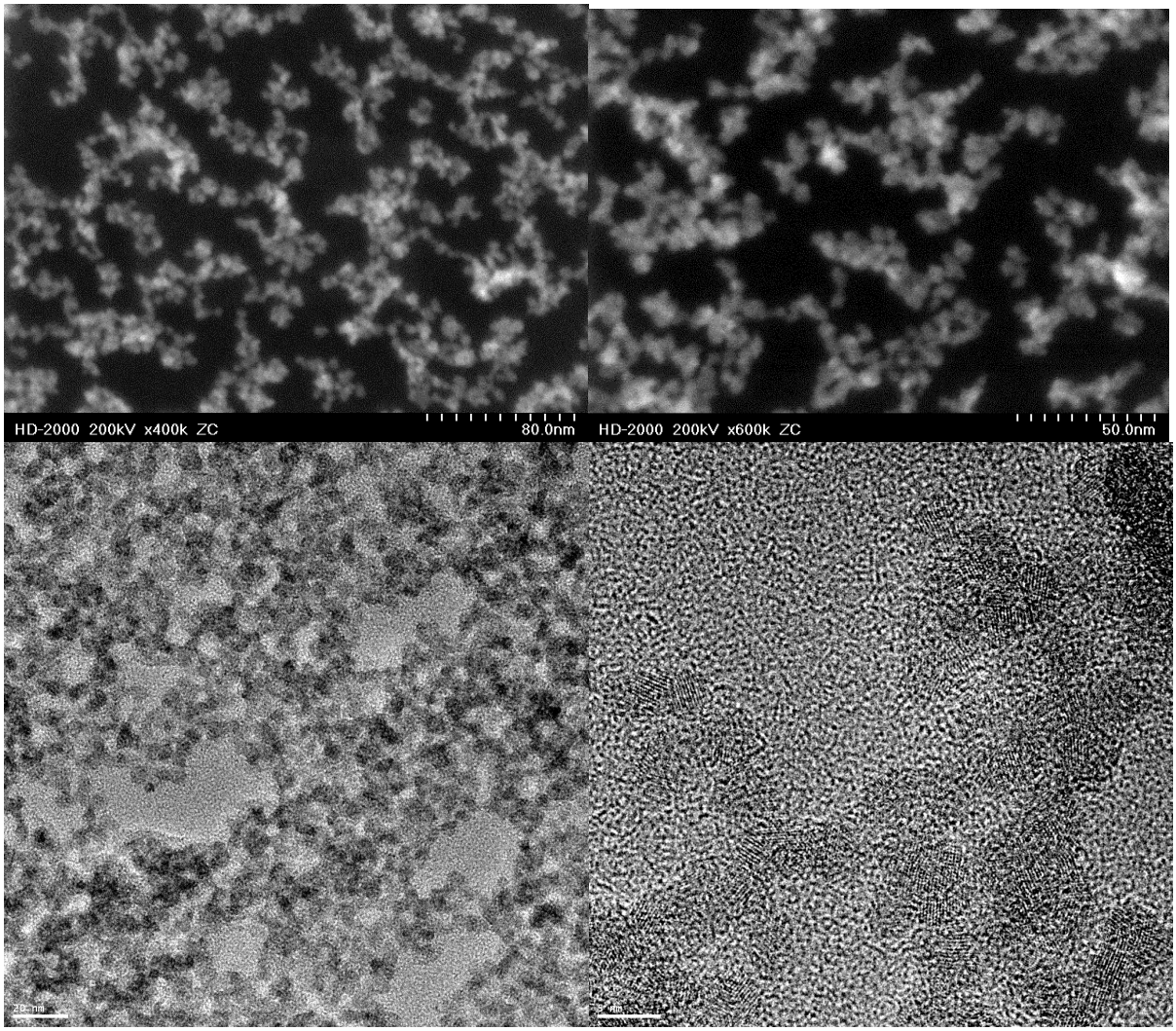

Figure S24: STEM and HR-TEM images of ZnO NPs from H_2O/H_2O_2 dispersion.

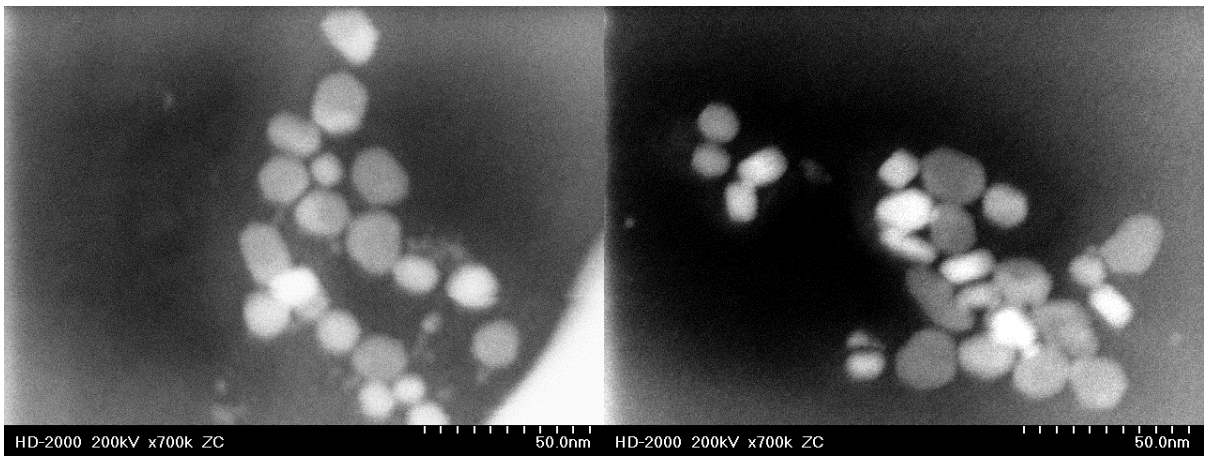

Figure S25: STEM images of $MgCo_2O_4$ NPs from H_2O/H_2O_2 dispersion.

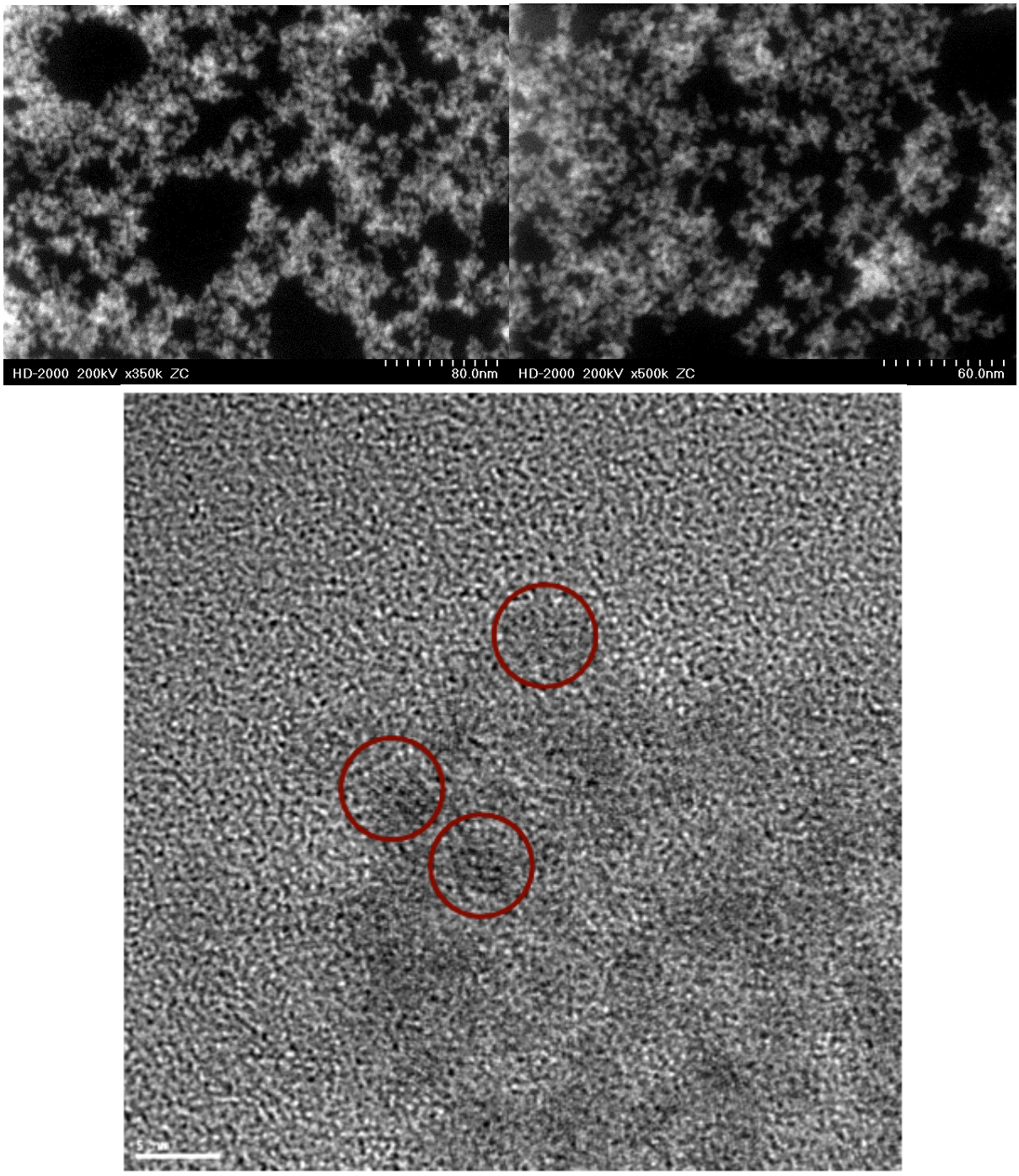

Figure S26: STEM and HR-TEM images of $MgZn_2O_4$ NPs from H_2O/H_2O_2 dispersion.

UV-Vis-NIR Spectra: The UV-Vis NIR spectra were recorded using thin films, obtained by spin coating of the dispersions over quartz slides and calcination at 450°C. The spectra were recorded using a Perkin Elmer Lamda 900 spectrophotometer in transmittance mode with a scan speed of 125 nm/min.

ZnO is a direct band gap semiconductor with a bulk band gap of 3.3 eV. The spectrum of the film displays a sharp absorption at around 345 nm originating from 1st excitonic transition. Note that ZnO has a large exciton binding energy (60 meV) and can be observed even at room temperature. There is a small blue shift on the band gap of our film (3.39 eV) and correspond to around 4 nm nanocrystallites. The sharp absorption edge is an indication for a narrow size distribution. The UV spectrum and the other supporting data are indicating that the films are made up of nanocrystallites (see for more details S.T. Tan, B. J. Chen, X. W. Sun, W. J. Fan, H. S. Kwok, X. H. Zhang, S. J. Chua *J. of Appl. Phys.* **2005**, *98*, 013405).

NiO is considered to be an indirect p-type semiconductor. The typical band gap is at around 3.5 eV and show size dependence. A small blue shift (to 3.60 eV) is observed in our film. The low energy tail in the visible region gives colouring to the film and originate from the Ni(III) sites that makes NiO p-type. (see for more details, G. Boschloo, A. Hagfeldt *J. Phys. Chem. B* **2001**, 105, 3039-3044).

MoO_3 is considered to be a direct gap semiconductor with a bulk band gap of 3.05. A large blue shift is observed from our film that has a band gap of 3.89 eV (see for more details, G. Hoppman, E. Salje *Opt. Commun.* **1979**, *30*, 199-202).

WO_3 is considered to be an indirect band gap (between 2.60 and 3.00 eV). Our film sample display an indirect band gap of 3.33 eV. The blue shift is due to quantum size effect and indicating the nanoscale nature of the film (see more details in P. P. Gonzalez, F. Sato, A. N. Medina, M. L. Baesso, A. C. Bento, C. Baldissera, C. Persson, G. A. Niklasson, C. G. Granqvist, F. da Silva *Appl. Phys. Lett.* **2010**, *96*, 061909).

The thin film of Co_3O_4 displays two different bands at 1.50 and 2.25 eV and weak crystal field transitions ($^4A_2$ to $^4T_1$) in the NIR region of the spectrum. The band to band transitions are due to oxygen to Co(III) and Co(II) (ligand to metal charge transfer), respectively. Co_3O_4 is considered to be direct gap p-type semiconductor. Our data is consistent with the observations in the literature. The UV-vis-NIR spectrum of the film also shows high purity and optical quality of the films. Typically these two band gaps are reported at 1.5 and 2.0 eV, respectively for the bulk Co_3O_4 crystals. (see for reference; D.

Barreca, C. Massignan, S. Daolio, M. Fabrizio, C. Piccirillo, L. Armaleo, E. Tondello *Chem. Mater.* **2001**, 13, 588-593).

The crystalline Fe_2O_3 has an indirect band gap of 2.14 eV. Our film displays an absorption edge that fits best with the indirect gap relation. It provides a band gap of 2.18 eV (B. Gilbert, C. Frandsen, E. R. Maxey, D. M. Sherman *Phys. Rev. B* **2009**, *79*, 035108).

Interestingly the $MgCo_2O_4$ spinel has a similar absorption spectra to that of Co_3O_4. Two band gaps are observed at 1.48 and 2.37 eV. The absorption edges in the visible and NIR must originate from the Co(III) and Co(II) sites in the nanocrystals.

MgO has a very large band gap, reported to be at 7.8 eV. The weak absorption tailing down to the visible region may originate from defects and dangling bonds.

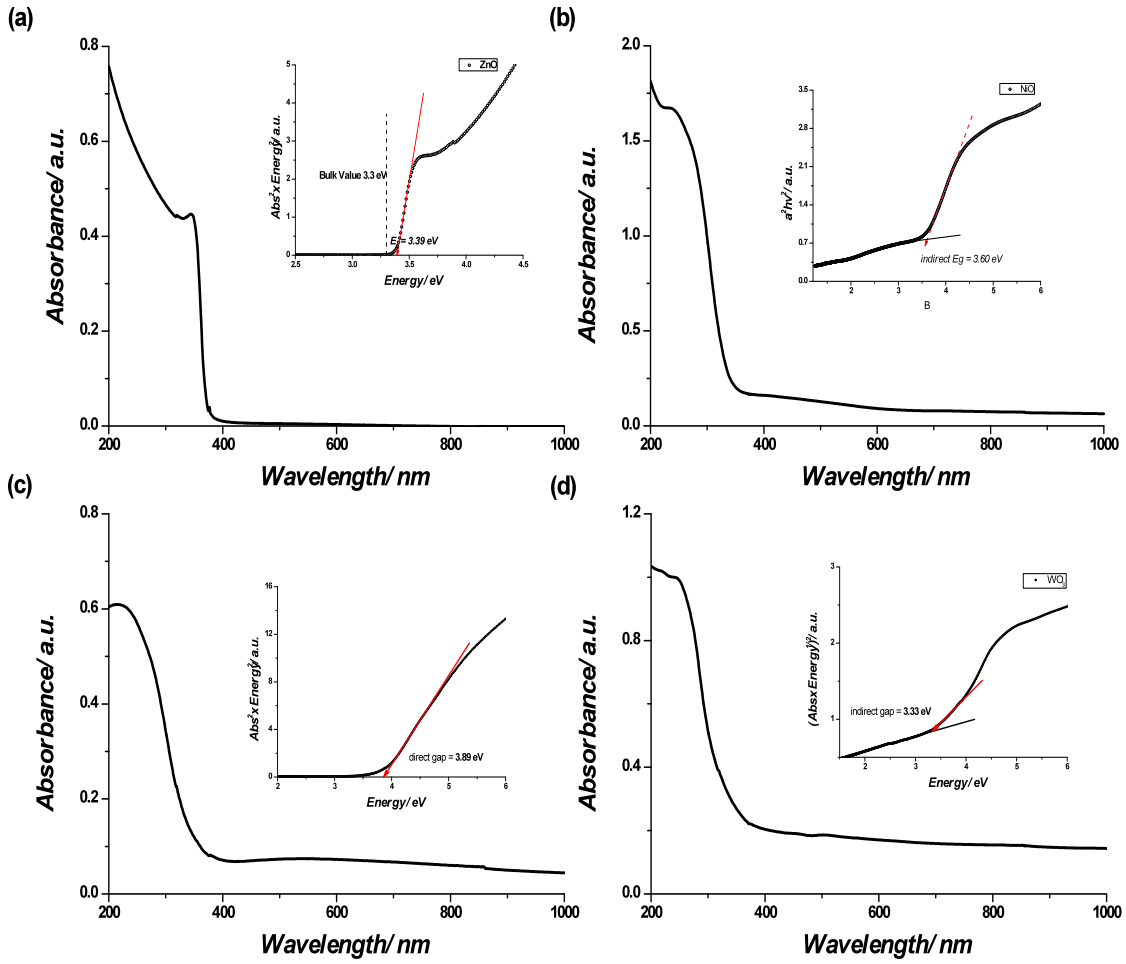

Figure S27: UV-Vis-NIR absorption spectra of (a) ZnO, (b) NiO, (c) $MoO_3.{}^1/_3\ H_2O$, and (d) $WO_3.{}^1/_3\ H_2O$ (Insets are the Tauc plots to evaluate band gaps).

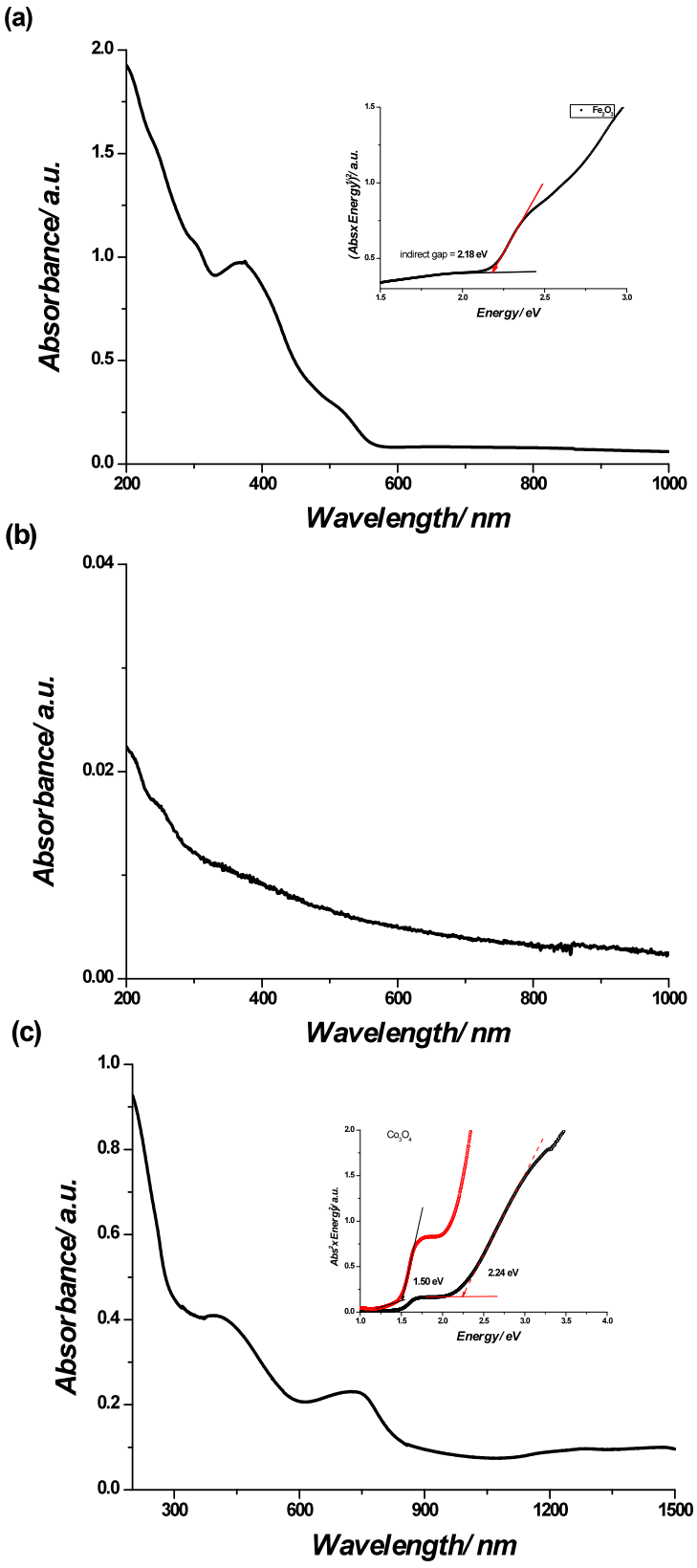

Figure S28: UV-Vis-NIR absorption spectra of (a) Fe_2O_3, (b) MgO, and (c) Co_3O_4 films (the corresponding band gaps are indicated in the insets).

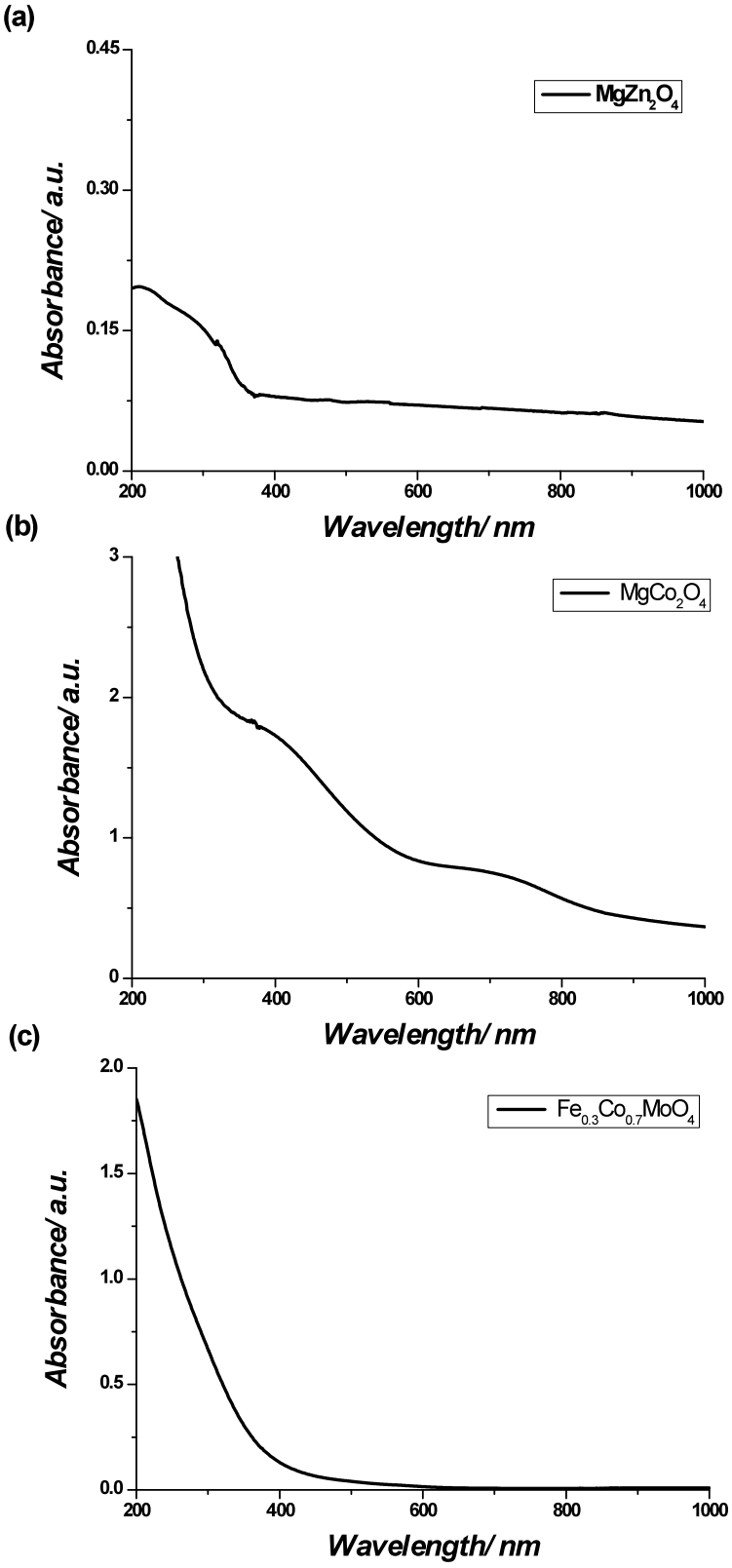

Figure S29: UV-VIS absorption spectra of the binary $M_1M_2O_4$ (spinel) and the ternary metal oxide films as indicated in the spectra.

The Raman spectra were recorded using LabRam 300 spectrometer equipped with a confocal microscope (100 μm slit width and 300 μm pin hole), 532 nm excitation laser (1 micron spot size), electronically cooled CCD camera and a 1200 grazes/mm monochromator.

The powder samples were obtained by drying the dispersions. Two sets of representative Raman spectra are shown in Figures S30 to S36. The first set is from the metal oxides that form in the solution and crystalline with a bulk oxide structure (Figures S30, S31, S34, and S36). These samples display diagnostic metal oxide related Raman peaks (for details see references given in the figure captions for each metal oxides). The second set was obtained by drying the dispersions that are formed from the metal peroxide and superoxide with acetate surface species. The acetate ions likely compensate the surface charge on the particles. To eliminate the possibility of nickel acetate ($Ni(Ac)_2$) formation in the nickel oxide, zinc acetate ($Zn(Ac)_2$) formation in the ZnO_2, and magnesium acetate ($Mg(Ac)_2$) in the MgO_2 samples, we also recorded the Raman spectra of $Ni(Ac)_2$, $Zn(Ac)_2$, and $Mg(Ac)_2$. The acetate related peaks in our sample is either broader or shifted, indicating that the acetate species are on the surface of these particles and acting as capping agents. The remaining peaks are characteristic for the NiO, ZnO_2, and MgO_2 nanoparticles.

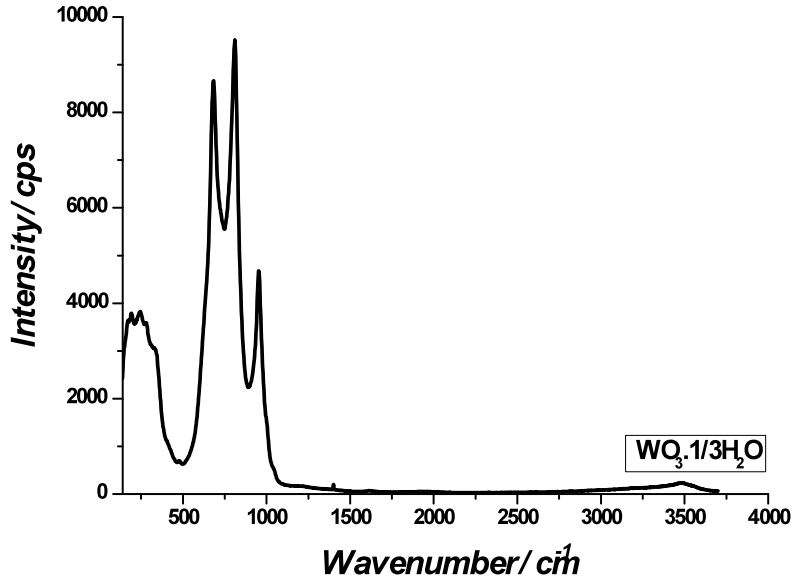

Figure S30: Raman spectrum of the dried $WO_3.{}^1/_3\ H_2O$ Sample. Reference Raman-Spectra and/or reference data can be found in: M. F. Daniel, B. Desbat, J.-C. Lassègues, *Journal of Solid State Chemistry*, **1987**, *67*, 235-247.

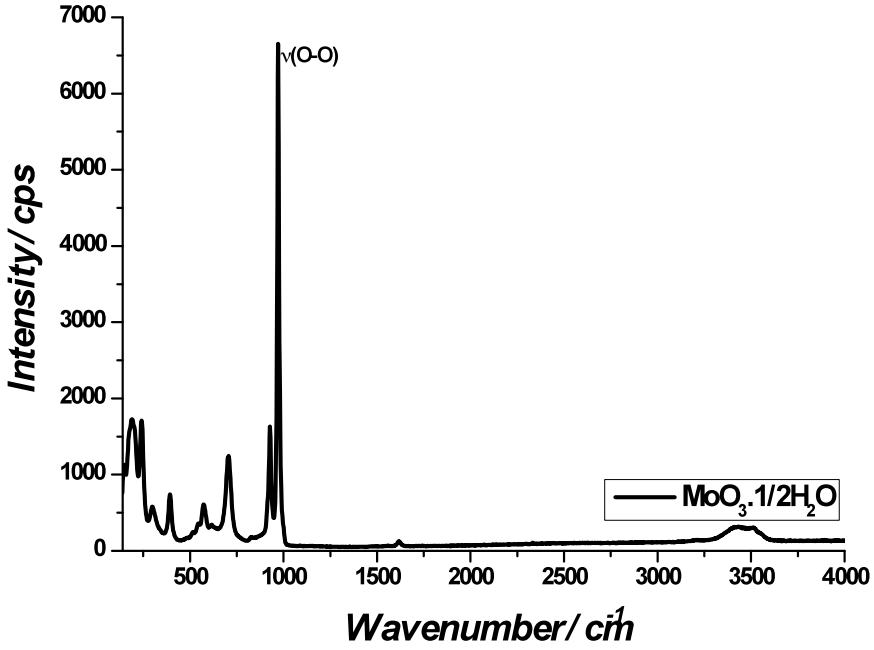

Figure S31: Raman spectrum of the dried $MoO_3.^1/_3\ H_2O$ Sample. Reference Raman-Spectra and/or reference data can be found in: L. Seguin, M. Figlarz, R. Cavagnat, J.-C. Lassègues, *Spectrochimica Acta Part A*, **1995**, *51*, 1323-1344.

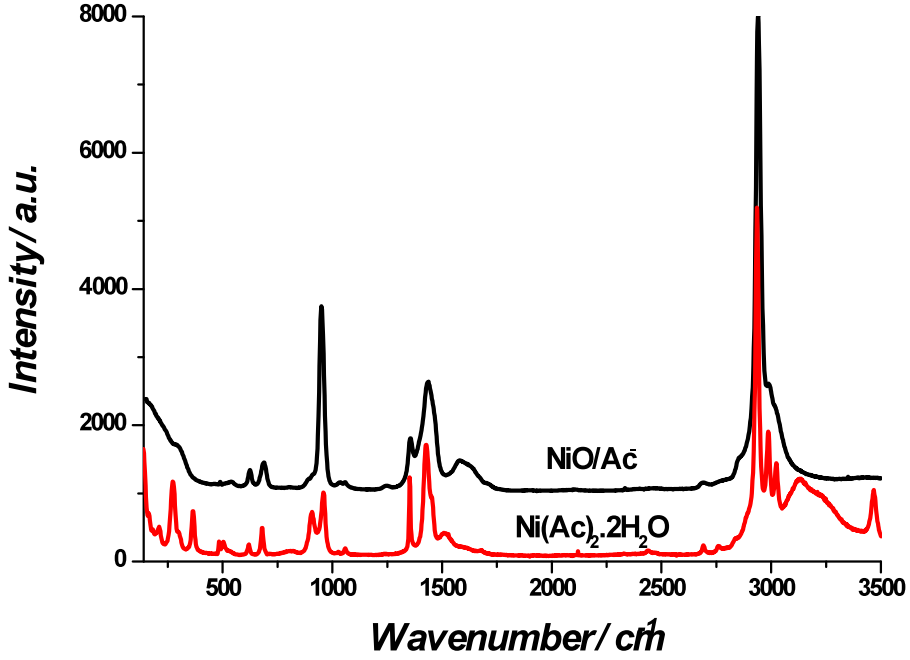

Figure S32: Raman spectra of the dried amorphous Ni-Oxide Sample and nickel acetate. Reference Raman-Spectra and/or reference data can be found in: N. Mironova-Ulmane, A. Kuzmin, I. Sildos, M. Präs, *Cent. Eur. J. Phys*, **2011**, 1-4. doi:10.2478/s11534-010-0130-9

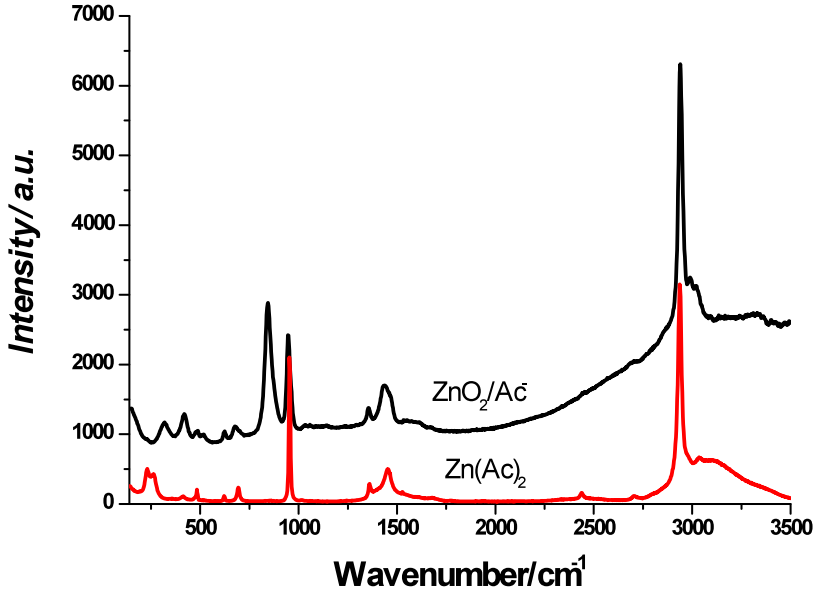

Figure S33: Raman spectra of the dried ZnO (ZnO_2) sample and zinc acetate. Reference Raman-Spectra and/or reference data can be found in: M. Sun, W. Hao, C. Wang, T. Wang, *Chemical Physics Letters*, **2007**, 443, 342-346.

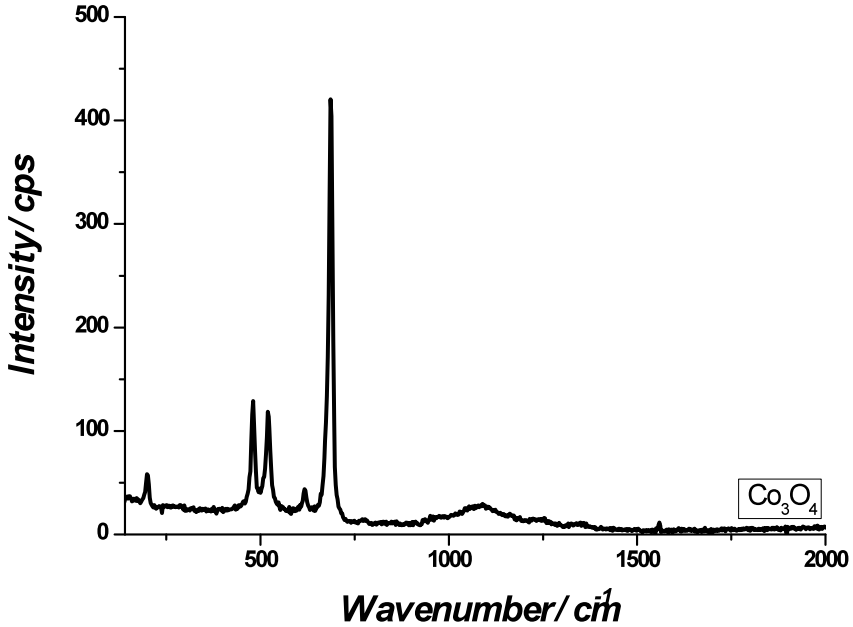

Figure S34: Raman spectrum of the dried Co-Oxide Sample. Reference Raman-Spectra and/or reference data can be found in: A. H. Jayatissa, K. Guo, A. C. Jayasuriya, T. Gupta, *Materials Science and Engineering B*, **2007**, *144*, 69-72.

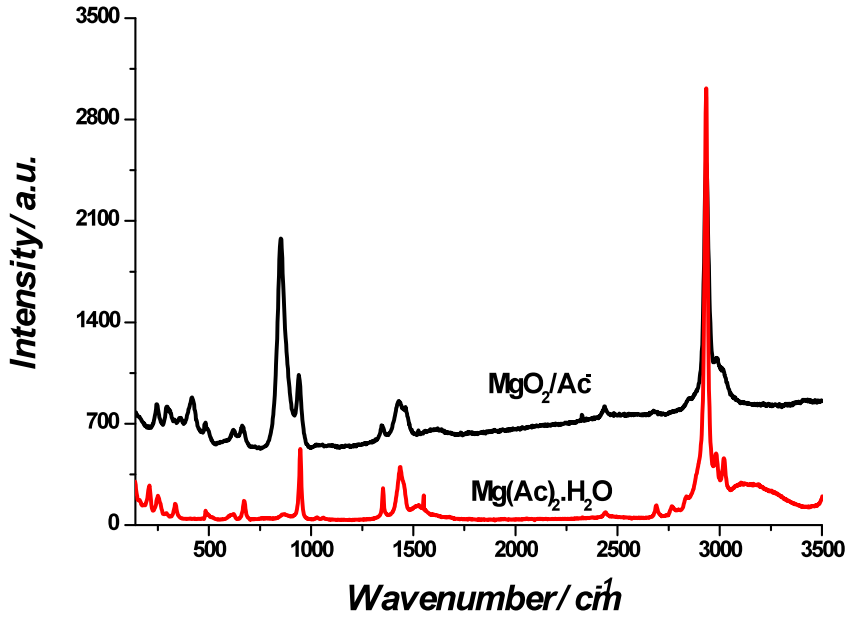

Figure S35: Raman spectrum of the dried MgO_2 (MgO) Sample. Reference Raman-Spectra and/or reference data can be found in: F. J. Blunt, P. J. Hendra, J. R. Mackenzie, *Chem. Comm.* **1969**, 278-279.

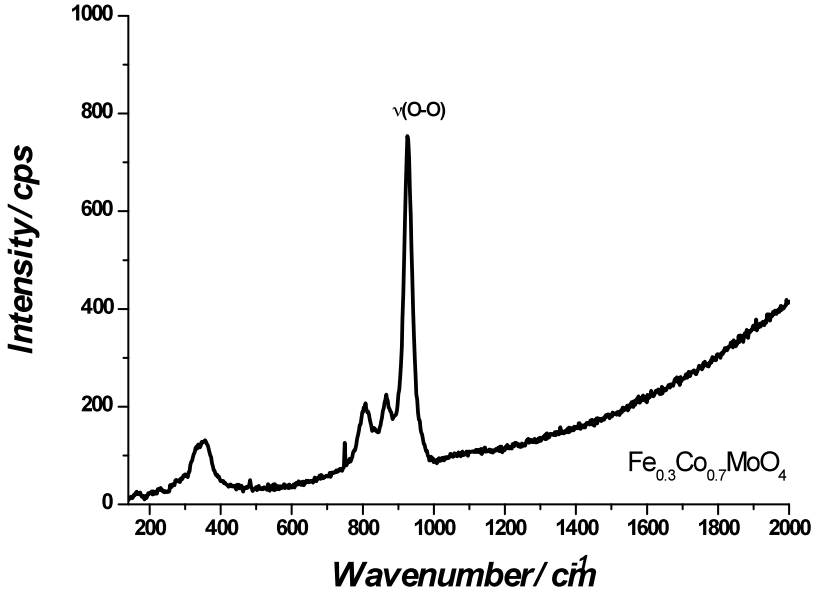

Figure S36: Raman spectrum of the dried $Fe_{0.3}Co_{0.7}MoO_4$.

Examples of surface zeta potential e.g. for the obtained Fe_2O_3 and ZnO dispersion were measured through electrophoretic mobility measurements on a ZetaSizer 3000 HSa, Malvern Instruments, Southborough, Boston, MA. A zeta potential transfer standard DTS 1230 (-68 ± 6.8 mV) was tested before measuring the samples. Prior to analysis, the respective metal oxide samples were diluted with deionized H_2O in the ratio of 10:1 to obtain optical transparency for the measurements. Particle zeta potential measurements were performed five times for consistency purposes. pH measurements were performed on a VWR SympHony SB70P laboratory pH meter

Run	Pos.	KCps	Mob.	Zeta	Width	Time
1	17.0	609.1	3.499	44.1	6.4	14:05:07
2	17.0	594.6	3.608	45.6	6.5	14:06:46
3	17.0	631.9	3.570	45.1	6.5	14:08:11
4	17.0	653.5	3.217	40.6	6.5	14:09:24
5	17.0	716.9	3.933	49.6	6.5	14:10:40
Average		641.2	3.565	45.0	6.5	
+/-		47.9	0.257	3.2	0.0	

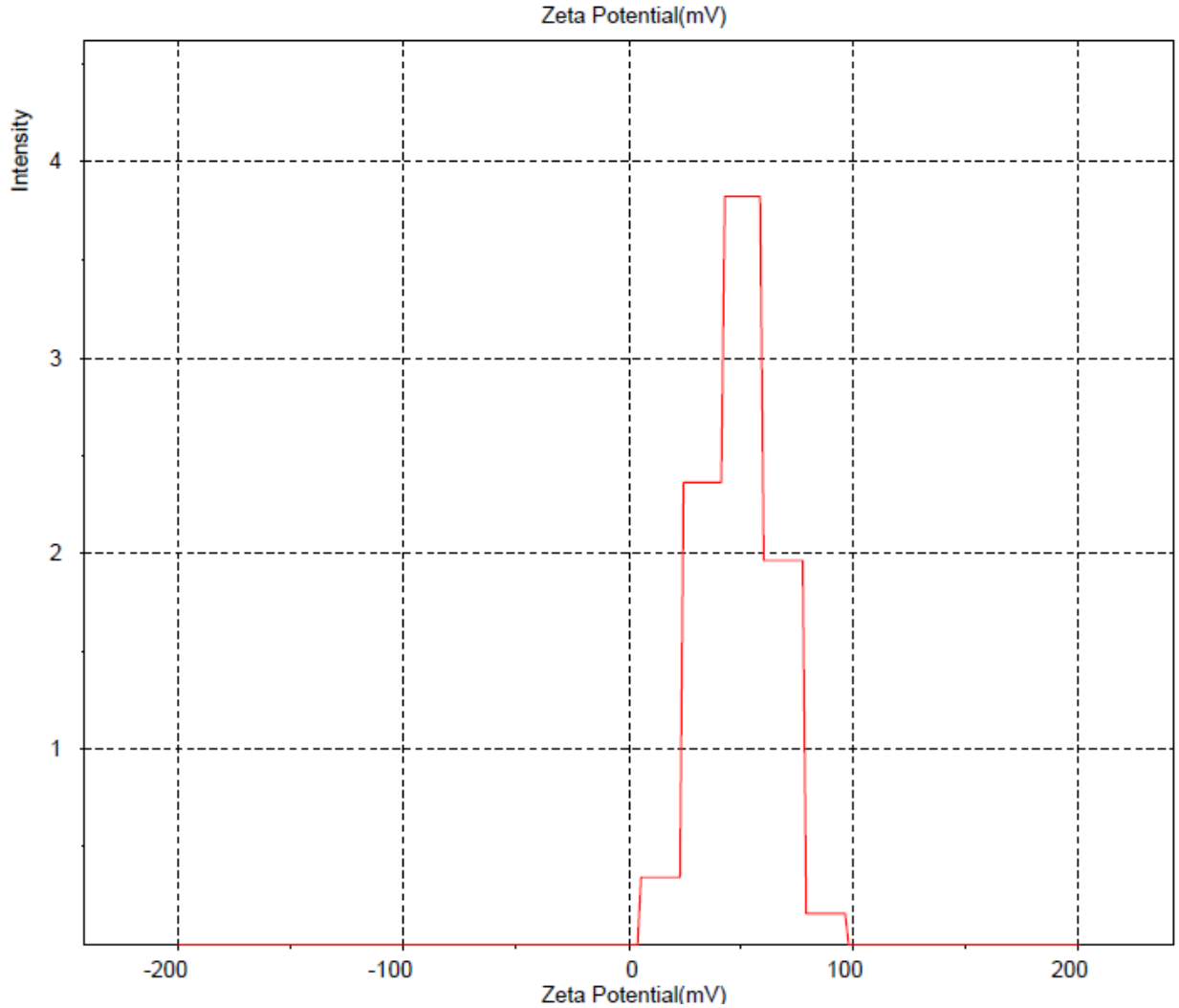

Figure S37: Surface Zeta potential of the Fe_2O_3 dispersion.

Run	Pos.	KCps	Mob.	Zeta	Width	Time
1	17.0	733.4	3.252	41.0	6.5	14:54:05
2	17.0	770.5	3.431	43.3	6.5	14:55:19
3	17.0	726.3	3.381	42.6	6.5	14:56:32
4	17.0	751.3	3.687	46.5	6.5	14:57:49
5	17.0	675.7	3.698	46.7	6.5	14:59:01
Average		731.5	3.490	44.0	6.5	
+/-		35.6	0.196	2.5	0.0	

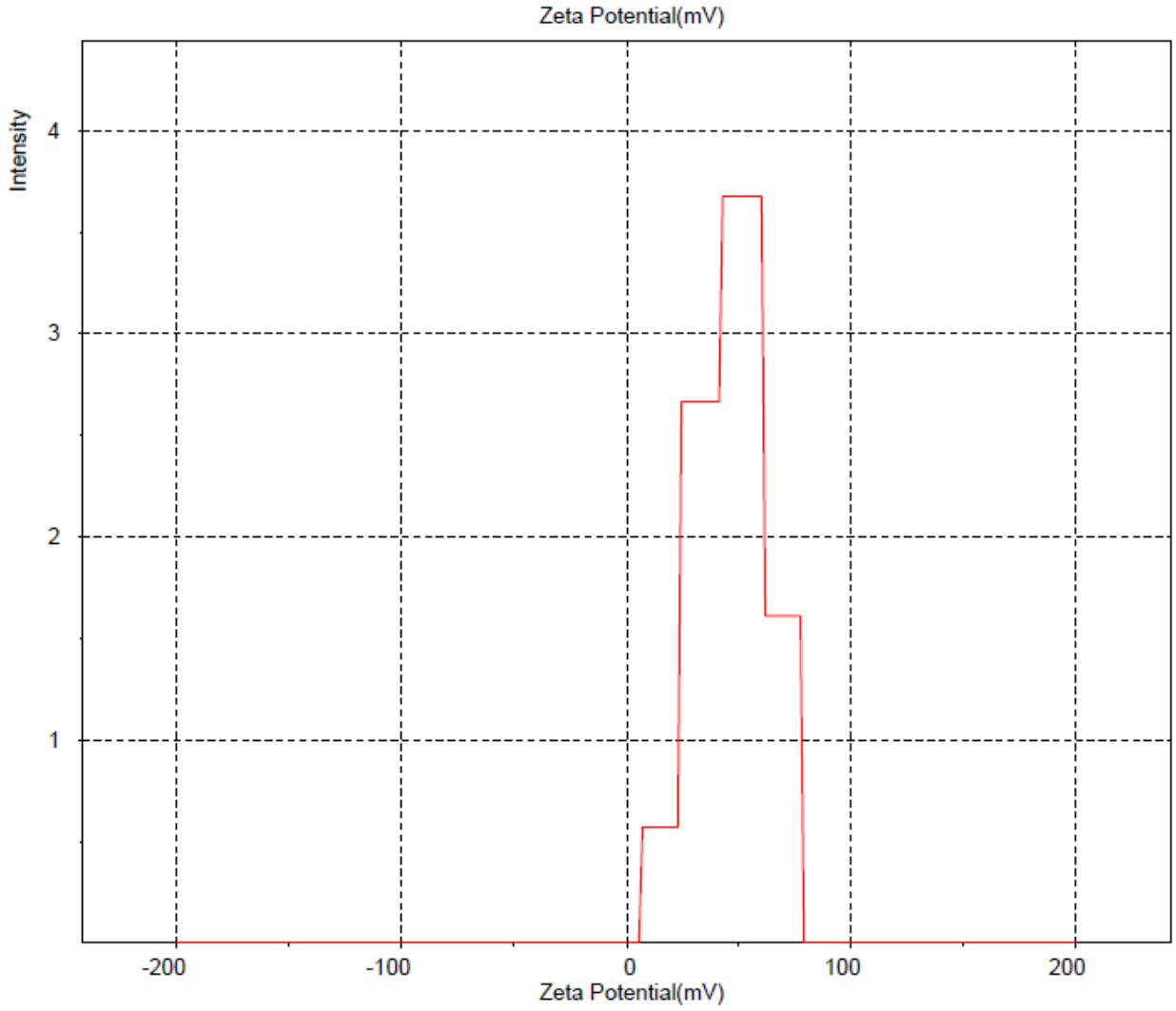

Figure S38: Surface Zeta potential of zinc oxide dispersion.

Scanning electron microscopy (SEM) images were obtained using a Hitachi S-5200 operating at 1-5 kV for films on silicon substrates, or at 30 kV for films scraped off onto a carbon-coated copper grid.

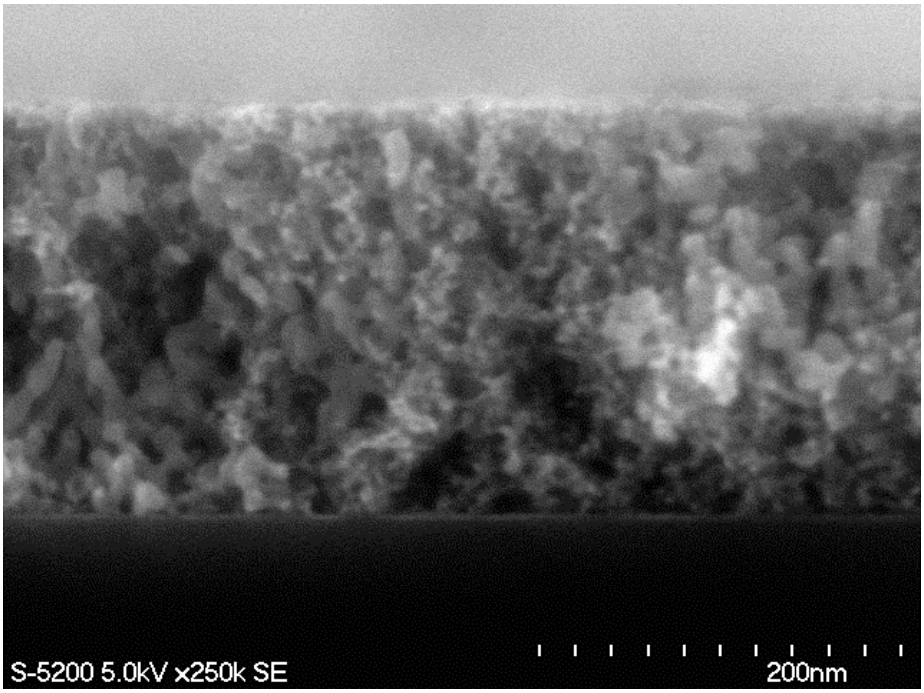

Figure S39: Example of a single porous □-Fe_2O_3 thin film.

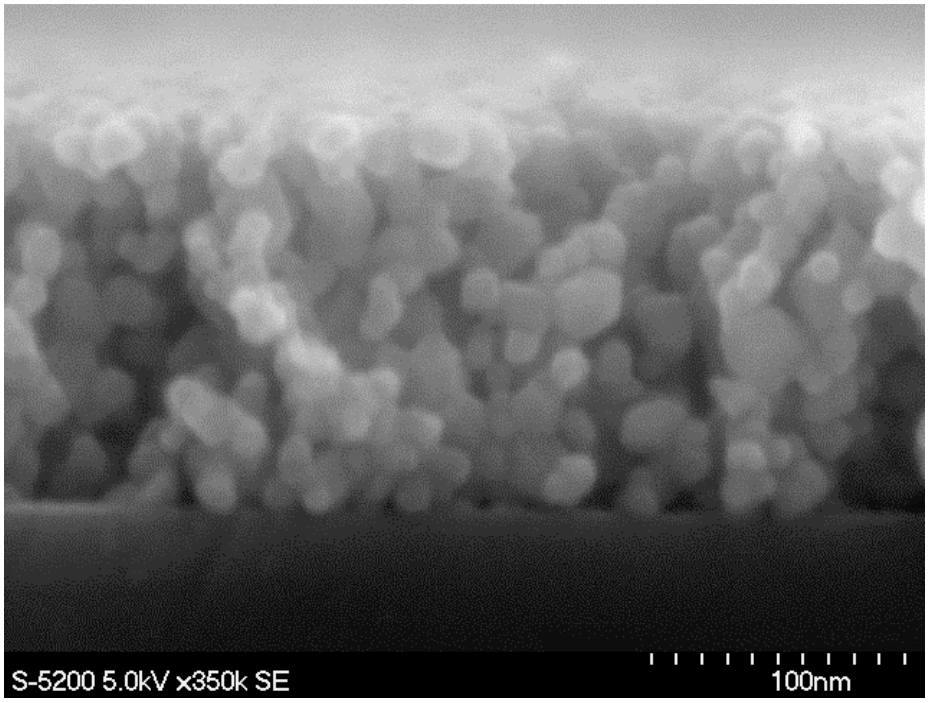

Figure S40: Example of a single porous Co_3O_4 thin film.

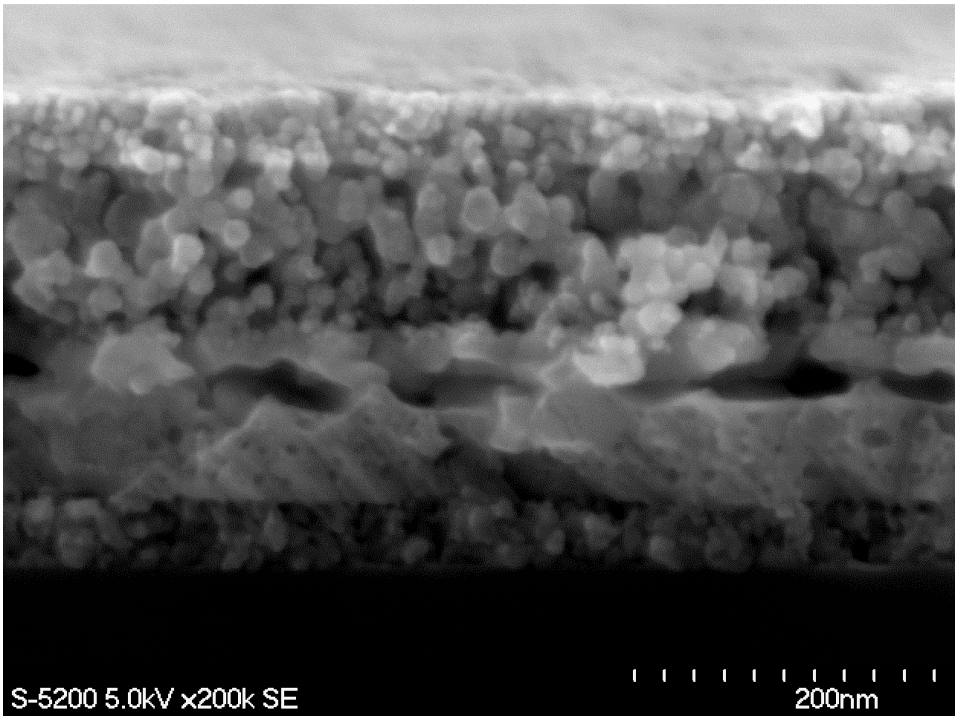

Figure S41: Example of a multilayer assembly of different porous metal oxide thin films with NiO (top layer); Co_3O_4, WO_3 and ZnO (bottom layer).

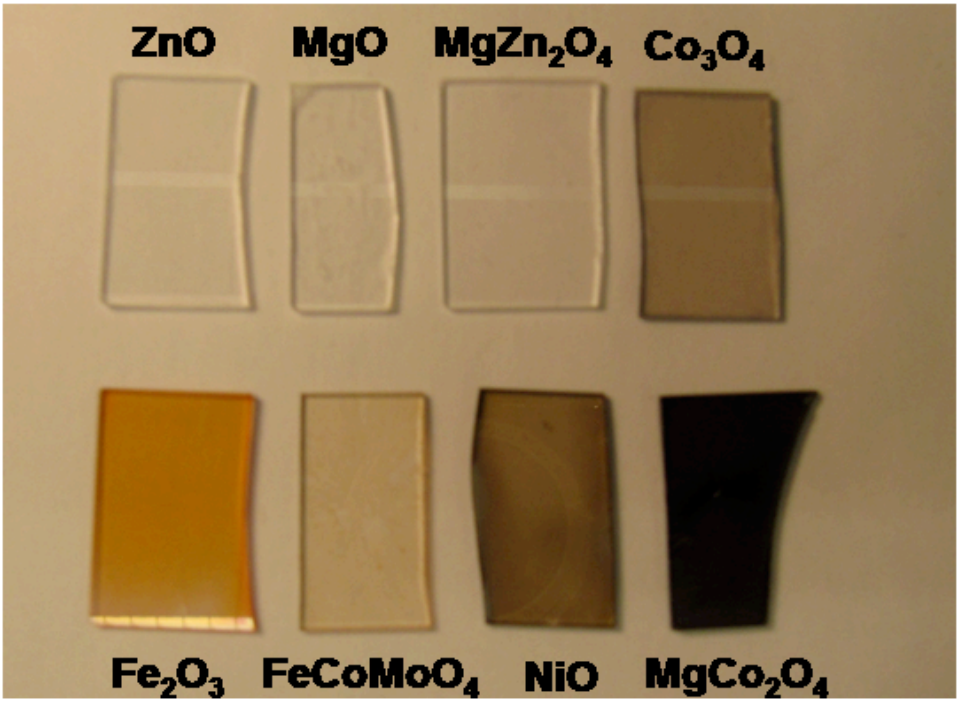

Figure S42: Example of a spin coated metal oxide thin films on quartz substrates, calcinated under air at 450ºC for 15-20 mins.